

IMAGES, STRUCTURAL PROPERTIES AND METAL ABUNDANCES OF GALAXY CLUSTERS OBSERVED WITH *Chandra* ACIS-I AT $0.1 < Z < 1.3$.

B. J. MAUGHAN^{1,†}, C. JONES¹, W. FORMAN¹, AND L. VAN SPEYBROECK¹
 Harvard-Smithsonian Center for Astrophysics, 60 Garden St, Cambridge, MA 02140, USA.
Draft version September 10, 2018

ABSTRACT

We have assembled a sample of 115 galaxy clusters at $0.1 < z < 1.3$ with archived *Chandra* ACIS-I observations. We present X-ray images of the clusters and make available region files containing contours of the smoothed X-ray emission. The structural properties of the clusters were investigated and we found a significant absence of relaxed clusters (as determined by centroid shift measurements) at $z > 0.5$. The slope of the surface brightness profiles at large radii were steeper on average by 15% than the slope obtained by fitting a simple β -model to the emission. This slope was also found to be correlated with cluster temperature, with some indication that the correlation is weaker for the clusters at $z > 0.5$. We measured the mean metal abundance of the cluster gas as a function of redshift and found significant evolution, with the abundances dropping by 50% between $z = 0.1$ and $z \approx 1$. This evolution was still present (although less significant) when the cluster cores were excluded from the abundance measurements, indicating that the evolution is not solely due to the disappearance of relaxed, cool core clusters (which are known to have enhanced core metal abundances) from the population at $z \gtrsim 0.5$.

Subject headings: cosmology: observations – galaxies: clusters: general – galaxies: high-redshift galaxies: clusters – intergalactic medium – X-rays: galaxies

1. INTRODUCTION

The study of galaxy clusters provides important insight into the formation of structure in the universe and allows tight constraints to be placed on cosmological parameters. Observations at different wavelengths probe complementary aspects of clusters' properties. In optical bands, the properties of individual cluster galaxies are studied and the measurement of their velocities enable the estimation of the total binding gravitational mass, via the application of the virial theorem (e.g. Zwicky 1937). Observations at optical wavelengths also allow cluster mass estimates via strong and weak lensing analyses (e.g. Lynds & Petrosian 1989; Tyson et al. 1990).

At longer wavelengths, radio observations of clusters have important applications. The inverse Compton scattering of cosmic microwave background photons by the energetic electrons in the intra-cluster medium (ICM) gives rise to the Sunyaev Zel'dovich effect (SZE; e.g. Birkinshaw 1999). Observations of this effect can be used to detect clusters and probe the properties of the ICM. Radio-emitting jets from active galactic nuclei (AGN) interact with the ICM, inflating cavities and driving shocks in the X-ray gas, and are likely to have an important impact on ICM properties (e.g. McNamara et al. 2000).

The most sensitive measurements of the ICM properties are currently made at X-ray wavelengths. The ionised gas of the ICM is the dominant baryonic component of galaxy clusters, and X-ray observations yield fundamental properties of the ICM such as X-ray luminosity and temperature, and permit mass estimates (assuming the gas is in hydrostatic equilibrium) even for clusters at high redshifts (see Sarazin 1986, for a review). In the local universe it has been found that most ($\sim 2/3$) clusters

host cool cores (Peres et al. 1998; Vikhlinin et al. 2006). The high gas densities in these core regions give rise to efficient radiative cooling with corresponding bright peaks in the X-ray emission and suppressed temperatures. Early models predicted that large amounts of gas should cool out of the ICM in this process, although the fate of the condensing material was unknown (e.g. Fabian 1994). More recent *XMM-Newton* observations have found that the majority of the core gas does not cool out of the X-ray emitting regime, requiring some form of heating to regulate the process (Peterson et al. 2001). AGN feedback is a strong candidate for providing this energy input (e.g. Nulsen et al. 2005). The gas cooling in cool cores is still significant however; core temperatures of $\sim 30\%$ of the global value are typical, with detectable cooling extending to $\sim 0.15R_{500}$ (e.g. Vikhlinin et al. 2005; Sanderson et al. 2006)².

While cool cores are common features in relaxed systems, clusters are observed in a variety of dynamical states, and X-ray observations allow cluster morphologies to be studied. Early work categorised clusters into different classes based on their appearance (Jones & Forman 1984; Jones & Forman 1999), while more quantitative methods have been developed enabling cluster morphologies to be correlated with other properties (e.g. Buote & Tsai 1995; Mohr et al. 1993). Using such methods, evidence has been found that clusters are generally less relaxed at $z > 0.5$ (Jeltema et al. 2005). X-ray imaging analysis has also been used recently to demonstrate that the fraction of cool core clusters in the population drops from $\approx 65\%$ locally to $\sim 15\%$ at $z > 0.5$ (Vikhlinin et al. 2006). These two observational findings are consistent with the higher merger rates expected at

Electronic address: bmaughan@cfa.harvard.edu

[†] *Chandra* fellow

² R_{500} is the radius enclosing a mean overdensity of 500 with respect to the critical density at the cluster's redshift.

high-redshifts.

Further insight into the ICM properties can be gained from the emission lines in the X-ray spectra of clusters. These are due to significant amounts of heavy elements in the gas. The observed metal abundances are consistent with models of the enrichment of the ICM by supernovae based on observed star formation rates (Ettori 2005). X-ray observations have enabled spatially resolved abundance measurements in clusters, showing sharply central peaks in cool-core clusters, and only mild abundance gradients in non cool-core clusters (e.g. De Grandi & Molendi 2001). Recent work has also found lower average ICM metal abundances at high redshifts than locally (Balestra et al. 2006).

The *Chandra* X-ray observatory, with its high spatial and spectral resolution, is well suited to the study of galaxy clusters. Imaging analyses and spatially resolved spectroscopy of the ICM can be performed without the complications of point source contamination and deconvolution of the telescope point spread function (PSF). An important contribution of *Chandra* to the study of galaxy clusters is its large public data archive. This enables the construction of large samples of clusters whose properties are determined in a consistent manner, allowing powerful statistical studies of cluster properties, their correlations, and their evolution. In this *paper* we present a catalogue of 115 galaxy clusters observed by *Chandra*. The construction of the sample and the data reduction methods are detailed in §2 and §3. Our image analysis and X-ray images of the clusters are presented in §4 and the spectral analysis and spectral properties of the clusters are given in §5. Notes on individual clusters are given in §6 and the results are presented and discussed in §7. A Λ CDM cosmology of $H_0 = 70 \text{ km s}^{-1} \text{ Mpc}^{-1}$ ($\equiv 100h \text{ km s}^{-1} \text{ Mpc}^{-1}$), and $\Omega_M = 0.3$ ($\Omega_\Lambda = 0.7$) is adopted throughout and all errors are quoted at the 68% level.

2. THE SAMPLE

The sample was assembled from all publically available *Chandra* data as of November 2006. The positions of all *Chandra* pointings were correlated with the NASA/IPAC Extragalactic Database (NED), and observations with a galaxy cluster or group listed in NED within $10'$ of the *Chandra* aimpoint were kept. This list of observations was then refined by selecting only those for which the detector was ACIS-I, a galaxy group or cluster was the target of the observation, and the object had a published redshift greater than 0.1. No lower mass limit was applied to the target objects, but the lower redshift cutoff and the choice of the ACIS-I detector limits the number of galaxy group size objects in the sample. This combination of detector and lower redshift cutoff was chosen to ensure that the cluster emission within the radius R_{500} (our measurement of R_{500} is discussed in §5) was within the field of view, allowing properties to be measured to that radius without extrapolation. Quantitatively, we required that $> 50\%$ of the area in the annulus $(0.9 - 1.0)R_{500}$ intersected with the active ACIS-I CCDs. All clusters at $z > 0.1$ met this requirement, with the exception of *PKS0745 - 191* (ObsID 6103) at $z = 0.103$, which was rejected from the sample accordingly. Observations were then examined individually and rejected if insufficient useful data were left after lightcurve filter-

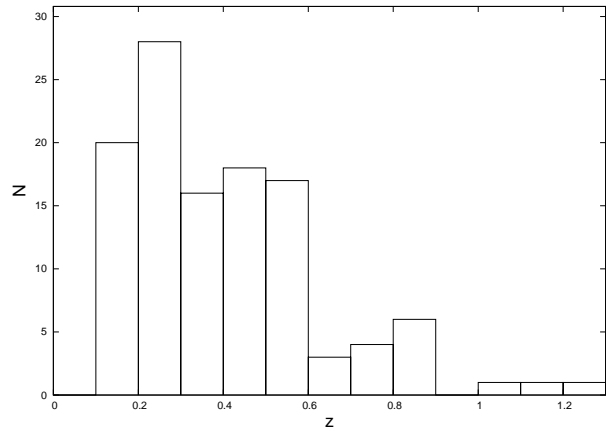


FIG. 1.— Redshift histogram of the final sample.

ing (described in §3), if they were affected by low level background flares (identified by inspection of the spectrum of the local background, as described in §5), or if no significant extended emission was detected at the cluster position. The latter was the case for a few candidate high-redshift clusters for which detections in earlier data (generally from *ROSAT*) were resolved into distinct point sources by *Chandra*.

The final sample then consisted of 149 observations of 115 galaxy clusters. The individual observations are summarised in Table 1. The clusters are listed in order of right ascension, and the positions given are the ICRS equatorial coordinates of the X-ray centroids. Column 2 gives the *Chandra* observation identifier for each observation and column 5 gives the redshift of each cluster (redshifts are taken from NED or BAX, the X-Rays Clusters Database). In columns 6 and 7 the date of each observation and corresponding “blank-sky” background period³ are given. Finally, column 8 lists the cleaned exposure time of each observation (the data cleaning process is described in §3). The redshift histogram of the final sample is shown in Fig. 1.

The clusters form a heterogeneous collection, having been observed for different purposes. Nearly half of the clusters (55) were observed in the guaranteed time observations of Leon Van Speybroeck as part of a program to combine X-ray data with SZE observations in order to place constraints on H_0 and Ω_M (Bonamente et al. 2006). One of the main goals in the current *paper* is to present a catalogue of the properties of this rich sample of clusters. The standardised methods that were used to analyse the data ensure that the results presented are self-consistent and can be duplicated in, for instance, comparative analyses of “mock observations” derived from numerical simulations. In follow-up papers we will investigate the X-ray scaling relations for this sample, including their evolution and scatter, and look in detail at clusters that deviate strongly from the trends measured for the sample as a whole.

3. DATA REDUCTION

Initially, the level 1 event files were reprocessed with the latest calibration (as of September 2006). If the fo-

³ See <http://cxc.harvard.edu/contrib/maxim/acisbg/>

cal plane temperature of the observation was cooler than -118.5°C then the charge-transfer inefficiency and time-dependent gain corrections were applied. For early observations with warmer focal plane temperatures, only the standard gain correction was used.

Background flare filtering was then performed with *lc_clean* in the 0.3–12 keV band for data from the ACIS-I CCDs, excluding the target CCD and all sources detected in the standard *Chandra* X-ray centre pipeline processing. Lightcurves were cleaned by 3σ clipping and periods with count rates $> 20\%$ above the mean rate were rejected. This is consistent with the cleaning applied to the blank-sky background datasets. The background dataset appropriate for the date of each observation was chosen, and if background period D was used, and the observation was taken in VFAINT telemetry mode, then the additional VFAINT cleaning procedure was applied to the source and background datasets⁴.

Finally, if the observation was not taken in the same detector configuration as the background files (ACIS-01236), then CCDs other than ACIS-0123 were removed from both source and background datasets. Otherwise CCD 6 was left in both the source and background files.

The use of blank-sky background data means that background data is available for the same detector regions as the source data. This eliminates systematic differences between the source and background data in both imaging and spectral analysis. However, the background consists of a particle-induced component which dominates at > 2 keV and varies with time, and a soft Galactic X-ray component which varies spatially over the sky. The contributions of these components in the blank-sky background will be different from those in the source dataset. These differences are accounted for in the imaging and spectral analysis methods described below.

An additional background dataset was produced for each observation to enable the subtraction of the ACIS readout artifact. While a CCD is being read out, source photons are still detected, creating a streak of source photons along the readout direction. The ratio of the readout time to the exposure time of one frame is 1.3%, so 1.3% of the source photons will be affected. Following the method described by Markevitch et al. (2000), we account for this effect by generating an additional background dataset from the source dataset, with the photon CHIP-Y positions randomised and coordinates and energies recalculated. This normalisation of this readout background is set to 1.3% of that of the source, and the blank-sky background normalisation is reduced accordingly. We note that the readout artifact was only significant for the clusters with very bright central peaks in their surface brightness distribution, but this correction procedure was applied to all data for consistency.

4. IMAGE ANALYSIS

4.1. Image preparation

Exposure maps were generated at an energy of 1.5 keV, chosen to correspond to the peak ACIS effective area. Point and extended sources in the field were detected using the wavelet detection algorithm of Vikhlinin et al. (1998). A broad band (0.3 – 7 keV) exposure-corrected

image was used for point source detection, while the 0.7 – 2 keV band was used for the detection of extended emission. The latter energy band was chosen to optimise signal to noise for typical cluster spectra and was used for all of the following imaging analysis. The centroid of the cluster emission was then located by refining its position with 5 iterations within $150''$ and then 5 iterations within $50''$ centered on the previous centroid (with point sources masked out). The target coordinates for each observation were used as the starting point for the iterations. This centroid was then used to define the position of the cluster throughout the analysis.

Extended sources that were detected as distinct separate sources compared to the target cluster were excluded, but any substructure that was detected in the cluster was left untouched. The division between separate extended sources and cluster substructure is not always simple, and in many cases redshifts were not available for different emission components. The thirteen clusters with excluded extended sources within R_{500} (in projection) are noted in §6.

Exposure-corrected radial profiles of the source and background images were then produced, with point sources excluded. An iterative process was followed to define the outer detection radius of the cluster emission and correctly normalise the background image in the imaging energy band. We defined the detection radius (r_d) as the outer radius of the last bin with a width between $5''$ and $150''$ in which emission was detected at $\geq 0.5\sigma$. While this is a weak criterion for detection, our purpose here is to be conservative in defining a source-free region in each observation, and the detection radii were confirmed by visual inspection of the source and background radial profiles. In each step of the iteration, the detection radius was determined, and a background scaling factor was defined as the ratio of source and background count rates in the imaging band, with the emission within r_d excluded. The background image was renormalised by this factor, and a new detection radius was computed. The process was repeated until r_d converged to within 1%. This method provides a robust normalisation of the background in the imaging band, and definition of the background emission in the source image.

The key assumption of this method is that some of the field of view is free of cluster emission. Visual inspection of the source and background radial profiles showed that this was the case even for the brightest clusters in the sample.

If the cluster emission were not fully excluded in this process, then the remaining cluster emission would cause the soft background level to be overestimated. This would result in a correlation between the derived background scaling and the cluster flux. This is plotted in Fig. 2, with the background scaling defined as the ratio of the source to blank-sky count rates in the background region in the imaging band (0.7 – 2 keV). The cluster fluxes were measured from the spectral analysis, using a different background correction (a scale factor derived at high energies; see §5) and so should be independent of the soft background scaling factor used here. A Spearman's rank test gives a $\sim 1\sigma$ correlation between background scaling and flux. However, this can be caused by a selection effect whereby fainter clusters are preferentially

⁴ <http://asc.harvard.edu/ciao/threads/aciscleanvf>

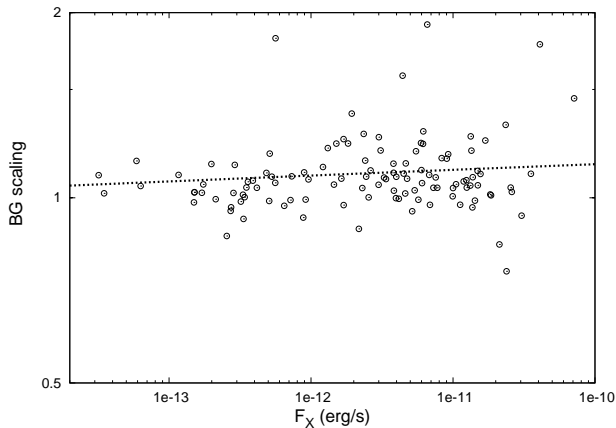


FIG. 2.— The 0.7 – 2 keV background scaling factor is plotted against cluster flux. The dotted line is the relation expected due to a selection effect of fainter clusters being preferentially observed in low background fields. The clusters with very high scale factors are those in regions of high Galactic foreground emission.

observed in fields with lower soft X-ray background levels.

This was tested by correlating the cluster fluxes and background scaling factors with the 0.75 keV X-ray background flux measured in the *ROSAT* all-sky survey (Snowden et al. 1997) in an annulus of 0.5 deg – 1 deg centered on each cluster. We found significant positive correlations between the soft X-ray background and both the cluster flux (at 93% probability) and our background scaling factor (99.99%). These two relations were then combined to predict the expected relation between background scaling and cluster flux under the hypothesis that any relation between those two variables is only due to the association of fainter clusters with lower background regions. This predicted relation is plotted in Fig. 2 and reproduces the weak trend found in the data. When this artificial correlation is factored out, any remaining trend is extremely weak, placing a limit of $< 1\%$ on the level of contamination of the background region by cluster emission. Note also that the clusters with large scale factors ($\gtrsim 1.4$) in Fig. 2 are those with very high levels of Galactic foreground emission, and are not affected residual cluster emission. This is illustrated in §5 and is corrected for in the imaging analysis by the simple scaling of the background image.

4.2. Surface brightness modelling

The background-subtracted, exposure-corrected X-ray surface brightness (S_X) profiles were then binned so that all radial bins were significant at the 3σ level and were fit with a simple one dimensional (1D) β -model of core radius r_c and outer slope β (Cavaliere & Fusco-Femiano 1976),

$$S_X(r) = S_X(0) \left(1 + \left(\frac{r}{r_c} \right)^2 \right)^{-3\beta+1/2}. \quad (1)$$

Images of the clusters were then reduced in size to a square of side $4R_{500}$ (R_{500} is defined in §5.1) centred on the cluster centroid and fit with a two-dimensional (2D) elliptical β -model. The ellipticity of the model was defined as $e = (1 - b/a)$, where a and b are the semi-major

and -minor axes respectively. The background was modeled with a constant level, which was fit to the normalised background image. All models were convolved with an image of the telescope PSF generated for the detector position of each cluster centroid at an energy of 1.5 keV, and multiplied by the exposure map.

It is well known that the β -model is not generally a good description of cluster surface brightness profiles, with additional components required to match the sharp surface brightness peaks found in the cores of many clusters (*e.g.* Pratt & Arnaud 2002; Jones & Forman 1984) and evidence for steepening at large radii (Vikhlinin et al. 1999). The model retains some appeal, however, as it is simple to deproject analytically to estimate the gas density distribution. As discussed in §4.3, we use a more complex model to fit the cluster emission and derive gas density profiles. The β -model is used solely to allow us to investigate the steepening of the profiles at large radii, and provide a first measurement of the cluster morphologies via their ellipticity.

In order to measure the local surface brightness slope at R_{500} (β_{500}), the background-subtracted, exposure corrected profiles were grouped into logarithmic bins. A straight line was fit in log space to the data in the radial range $(0.7 < r < 1.3)R_{500}$ giving the best fit slope and its uncertainty. This slope is independent of the core properties of the clusters. For 8 of the faintest clusters, the emission was not detected significantly at $1.3R_{500}$, so β_{500} was not be measured for these clusters. The logarithmic slope is related to the slope of the standard β -model by $d \log(S_X)/d \log(r) = 1 - 6\beta$ (for $r \gg r_c$). We thus defined β_{500} as

$$\beta_{500} = \frac{1}{6} \left(1 - \left. \frac{d \log(S_X)}{d \log(r)} \right|_{r=R_{500}} \right). \quad (2)$$

The same procedure was used to measure β_{mod} , the slope at R_{500} of the 1D β -model that was fit to the entire profile. The measured ellipticities and surface-brightness profile slopes are given in Table 2.

4.3. Gas density profile

The X-ray emissivity of the intra-cluster medium depends strongly on the gas density and only weakly on its temperature. This means that the observed projected emissivity profile can be used to accurately measure the gas density profile. For each annular bin in the surface brightness profile, the observed net count rate was corrected for area lost to chip gaps, bad pixels and excluded regions, and converted to an integrated emission measure. The conversion factor was calculated for each bin assuming an absorbed MEKAL (Kaastra & Mewe 1993) plasma model folded through an ARF generated for that region, and an on-axis RMF. The absorption of the spectral model was set at the galactic value and the metal abundance was set at 0.3. As the data are not sufficient to allow temperature profiles to be measured for most of the clusters in the sample, the temperature of the spectral model in each radial bin was obtained from the mean temperature profile found by Vikhlinin et al. (2005), normalised to the global temperature measured for each cluster (see §5.1). As noted above, the dependence of the conversion from count rate to emission mea-

sure on the assumed temperature is weak. The conversion factor decreases by $\sim 15\%$ when the model temperature is increased from 3 keV to 10 keV, with most of the decrease occurring below ~ 4 keV. Our analysis was repeated assuming the cluster was isothermal for the purpose of deriving the emission measures, and the results were not significantly changed.

The resulting profiles were fit with a modified version of the standard 1D β -model as proposed by Vikhlinin et al. (2006, hereafter V06) (see Pratt & Arnaud 2002, for other variations on the β -model);

$$n_p n_e = \frac{n_0^2 (r/r_c)^{-\alpha}}{(1 + r^2/r_c^2)^{3\beta-\alpha/2}} \times (1 + r^\gamma/r_s^\gamma)^{-\epsilon/\gamma}. \quad (3)$$

The first term modifies a β -model to include a power-law cusp with slope α at $r \ll r_c$. The second term allows a change of slope by ϵ at radius r_s ($r_s > r_c$) across a transition region whose width is controlled by γ . Following V06, γ was fixed at 3 for all fits. In order to simplify the model slightly, so that it could be used to fit the range of high and lower quality data in the sample we ignore a second β -model component included in the V06 models for some of their clusters.

This model was then projected along the line of sight and fit to the observed projected emission measure profile. The effect of the small *Chandra* PSF was neglected in this analysis. There are strong correlations between the parameters in the emission measure model so the individual parameters are not reported here. However, the gas masses derived from the best fitting models are given in Table 3, with uncertainties determined from Monte-Carlo randomisations of the observed emission measure profiles.

4.4. Centroid shifts

Various methods have been used to quantify the amount of substructure in cluster images. Power ratios derived from different moments of the surface brightness distribution have been found to be a useful diagnostic of cluster morphology (Buote & Tsai 1995). Centroid shifts measured from the variation in separation between the peak and centroid of cluster emission with aperture size have similarly been used to measure cluster morphologies (e.g. Mohr et al. 1993; O'Hara et al. 2006). Poole et al. (2006) used numerical simulation of cluster mergers to test the effectiveness of these methods and found that the centroid shift method was the most sensitive to the dynamical state of clusters and the least sensitive to noise in the cluster images. We thus adopt the centroid shift as our preferred statistic.

Centroid shifts were measured following the method of Poole et al. (2006). The centroid of the cluster emission was determined in a series of circular apertures centred on the cluster X-ray peak. The radius of the apertures were decreased in steps of 5% from R_{500} to $0.05R_{500}$ and the centroid shift, $\langle w \rangle$, was defined as the standard deviation of the projected separations between the peak and centroid in units of R_{500} . To increase the sensitivity of this statistic to faint structure, the central 30 kpc was excluded for the centroid (but not the X-ray peak) measurements. The measured centroid shifts are summarised in Table 2. The errors quoted for the $\langle w \rangle$ are the statistical uncertainties on a standard deviation calculated

from n measurements ($\langle w \rangle / (2n - 2)$).

Centroid shifts were measured from exposure-corrected images in order to eliminate the effects of chip gaps, and vignetting. The high spatial resolution of *Chandra* means that point sources could be excluded without significantly biasing the measured centroid position. As the purpose of the statistic is to quantify substructure, all extended sources were left untouched. The redshifts of many of the extended sources detected around the target clusters are unknown, so those sources known to be foreground or background objects were not excluded in order to treat all clusters consistently. In fact, as detailed in §6, only 13 of the 115 clusters had distinct extended sources that are projected within R_{500} of the cluster core and just one of those (V1701+6414) is known to be at a redshift different from the target cluster.

4.5. Contour maps

In order to examine the morphologies of the clusters, contour maps of the X-ray emission were generated using images that were adaptively smoothed to 3σ significance with the smoothing algorithm *asmooth* (Ebeling et al. 2006, we modified the original algorithm slightly to include exposure correction). The raw images were produced in the 0.7 – 2.0 keV band and were binned by a factor of 2, giving approximately $1''$ pixels. The images were then cropped to a box 3 Mpc on a side centred on the cluster's X-ray centroid. To correct for vignetting, CCD gaps and exposure variations in combined observations, exposure maps were provided to the smoothing algorithm.

To enable the statistical significance of morphological features to be determined from the contour plots, we selected contour levels to bound regions that were detected at a significant level above the local emission. The methodology is explained in detail in Maughan et al. (2007), but briefly, the emission enclosed between a contour and the one above it is detected at $> 3\sigma$ significance (after exposure correction) with respect to the emission between the contour and the one below it. In the case of the lowest contour, the emission is detected at $> 3\sigma$ above the background emission in the same region (measured in the blank-sky images). Note that this contouring scheme means that contour levels cannot be interpreted in the same way as in standard contour plots; separate contours that are the same number of levels above the background are unlikely to correspond to the same flux level in the smoothed image.

Fig. 3 shows example contour plots for a sample of the clusters. The plots for the full set of clusters are available in the electronic version of this paper. In addition, for each cluster, a region file containing the contours is available as online data⁵. The intention is that these provide a useful resource enabling contours of the X-ray emission to be easily overlaid on images obtained from other detectors. The region files also contain the flux levels of each contour to aid in their interpretation.

5. SPECTRAL ANALYSIS

In order to monitor the spectrum of the background emission in each observation, a spectrum was extracted from the source-free region and from the same region

⁵ <http://cxc.harvard.edu/cda/Contrib/2007/MAUG1>

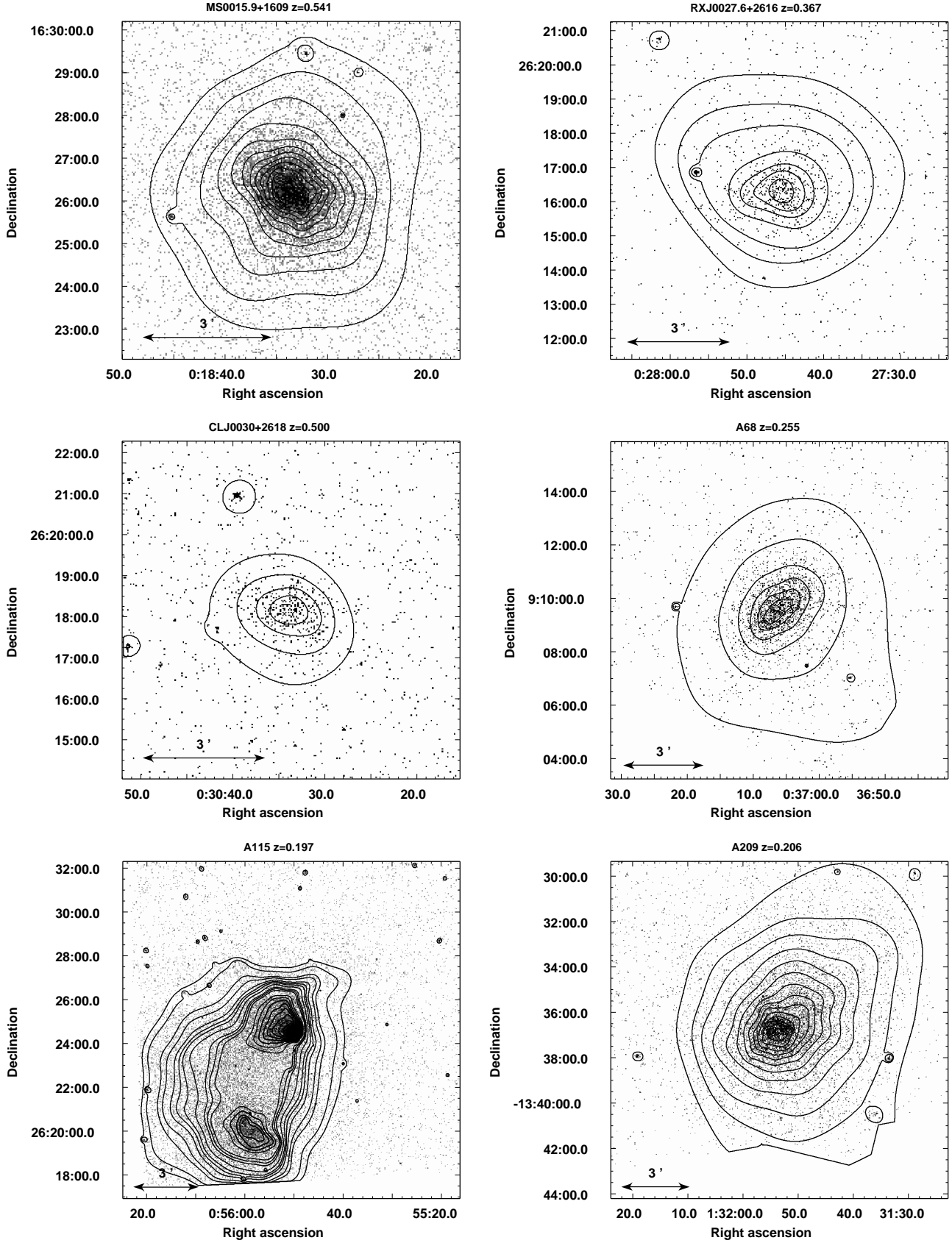


FIG. 3.— X-ray images of the clusters in the 0.7 – 2 keV band. The images are 3 Mpc on a side and are overlaid with contours of the same emission adaptively smoothed to 3σ . The contour levels c_i and c_{i+1} are set so that the emission bounded by those levels is detected at a significance of $> 3\sigma$ above the emission between levels c_{i-1} and c_i (see text for details).

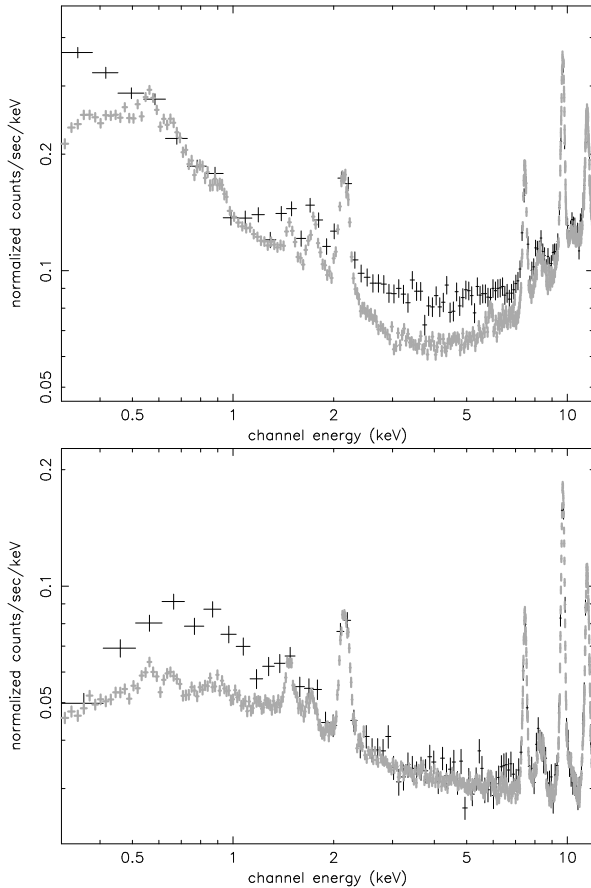


FIG. 4.— Blank-sky (grey) and local (black) background spectra are plotted for V1701+6414 (top) and for A1942 (bottom). The observation of V1701+6414 was affected by low level background flares, the effect of which can be seen in the elevated 2–7 keV continuum. The blank sky backgrounds could not be used for spectral analysis here. The observation of A1942 is a more typical example where the blank-sky and local background spectra agree well except for the Galactic foreground emission at < 2 keV.

in the blank-sky background. These spectra were compared to test the validity of using the blank-sky background spectrum for the analysis of that dataset. In order to account for differences in the particle-induced hard background, the background spectra were normalised to match the count rate in the 9.5 – 12 keV band in the source datasets. After this normalisation, an excellent agreement was generally found, except below ~ 2 keV due to differences in the soft Galactic foreground emission between the target and blank-sky fields. In rare cases, significant differences were found in the level of the continuum emission at 2 – 7 keV due to low level background flares that were not detected by the standard lightcurve filtering. If there were other, unaffected observations of the same target, then the data with low flares were rejected. For two clusters (A1682 and V1701+6414) there was no alternative data, and so a local background spectrum was used for the spectral analysis. Background spectra are shown in Fig. 4 for V1701+6414 and for A1942, a more typical example where the blank-sky and local background spectra agree well except for the Galactic foreground emission at < 2 keV.

In order to account for the differences in the soft background, the blank sky and readout background spectra were then subtracted from the local background spec-

trum to give a “soft residual” spectrum. These residuals were generally positive, indicating a higher soft background flux in the target pointings than the blank-sky fields, but in some cases were negative. The soft X-ray background is thermal in origin, and while the residual spectrum is the difference between thermal spectra, it is dominated by the oxygen lines at ~ 0.6 keV and is adequately described by a 0.18 keV APEC (Smith et al. 2001) model with zero redshift and positive or negative normalisation (Vikhlinin et al. 2005). The best fitting model to the soft residuals was included as an additional background component in all fits to cluster spectra, with the normalisation scaled for the differences in extraction area.

For all spectral fits, the source emission was modelled with an absorbed APEC model in the 0.6 – 9 keV band. The temperature, metal abundance and normalisation of the hot component were free to vary, while the absorbing column was fixed at the Galactic value inferred from 21 cm observations (Dickey & Lockman 1990). The model was refit with the soft Galactic component normalisation set to $\pm 1\sigma$ and again with the overall blank-sky background renormalised by $\pm 2\%$, and the resulting systematic temperature uncertainties were added in quadrature to the statistical uncertainties. For each source spectrum that was fit, the amount of flux lost to any excluded point and extended sources was estimated using the azimuthal average of the exposure-corrected, background subtracted flux at that cluster-centric radius. While this assumes azimuthal symmetry for the clusters, it is an improvement over a simple geometric flux correction that would not take into account the radially varying surface brightness distribution of the cluster.

5.1. Determination of R_{500}

Cluster properties were measured within the radius R_{500} . This radius generally matches the detected extent of the clusters’ emission, and corresponds to approximately half of the virial radius. R_{500} was measured following the approach recommended by Kravtsov et al. (2006) to estimate R_{500} from Y_X , where Y_X is defined as the product of the cluster temperature and gas mass. Y_X provides a reliable method for estimating cluster masses (and hence R_{500}), as the $Y_X - M_{500}$ relation has low scatter, and the shape and scatter in the relation is insensitive to merging clusters (Kravtsov et al. 2006). This makes it ideal for our sample, which contains clusters with a wide range of dynamical states. The low-scatter of the $Y_X - M_{500}$ relation and its self-similar evolution have been verified for a subset of the clusters in this sample (Maughan 2007). R_{500} and Y_X were computed iteratively, measuring the temperature in the aperture $(0.15 < r < 1)R_{500}$ and the gas mass within R_{500} , computing a new Y_X , and hence estimating a new value of R_{500} . The process was repeated until R_{500} converged to within 1%. An initial temperature estimate of 5 keV was used to estimate the first value of R_{500} to begin the iteration.

In order to estimate R_{500} from Y_X we used the $Y_X - M_{500}$ relation measured for the Vikhlinin et al. (2006) sample of clusters

$$M_{500} = \frac{h}{0.72} \frac{^{5B_{YM}}_2 - 1}{C_{YM} E(z)^{a_{YM}}} \frac{Y_X}{6 \times 10^{14} M_\odot \text{ keV}}^{B_{YM}} \quad (4)$$

with $B_{YM} = 0.564$, $C_{YM} = 7.047 \times 10^{14} M_{\odot}$ and $a_{YM} = -2/5$ (A. Vikhlinin, priv. comm.). $E(z)$ describes the redshift evolution of the Hubble parameter, and is given by

$$E(z) = \Omega_M(1+z)^3 + (1 - \Omega_M - \Omega_{\Lambda})(1+z)^2 + \Omega_{\Lambda}(5)$$

By definition, R_{500} is then given by $4/3\pi R_{500}^3 = 500\rho_c(z)/M_{500}$. This observed $Y_X - M_{500}$ relation has a normalisation $\sim 15\%$ lower than that found in the simulations of KVN06, which may be due to the effect of turbulent pressure support which is neglected in the mass derivations for the observed clusters (KVN06). Adopting the normalisation from the simulations would have the effect of increasing R_{500} by $\sim 2.5\%$ ($\sqrt[3]{15\%}$), increasing M_{gas} by $\sim 15\%$ with a negligible effect on other properties.

The aperture of $(0.15 < r < 1)R_{500}$ within which temperatures were measured in defining R_{500} was chosen to exclude any effects of cool core emission in the clusters, and is consistent with the $Y_X - M_{500}$ relation used. Once R_{500} was determined, the cluster properties were also measured with the core emission included, and the values obtained for both apertures are given in Table 1. We found that exclusion of the core ($r < 0.15R_{500}$) removed $\sim 30\%$ of the flux in non cool-core clusters (and a larger fraction from clusters with cool cores). This meant that for 4 of the faintest clusters (RXJ0910+5422, CLJ1216+2633, CLJ1334+5031 and RXJ1350.0+6007), we were unable to measure a temperature in that aperture. For those clusters, all of the cluster emission ($r < R_{500}$) was used for the temperature measurements in estimating R_{500} . None of these clusters showed evidence for the presence of cool cores, so the effect of including the core emission on biasing the temperature should be negligible.

5.2. Combining observations

Twenty nine of the clusters in this sample were observed more than once by *Chandra*. In these cases, the observations were first analysed separately as described above, and then the data were combined for certain stages of the analysis. Source, background and exposure map images were projected onto a common coordinate system and summed. The source lists from the individual observations were combined and those sources were excluded. The summed images were then used for all imaging analysis.

Multiple observations were also combined for the spectral analysis. Source and background spectra were extracted as above for each individual observation. The spectra were then fit simultaneously as before with the temperature and metal abundance of the hot APEC components tied together. This method was followed when determining R_{500} and the global temperature.

6. NOTES ON INDIVIDUAL CLUSTERS

In this section we note any peculiarities or points of interest about individual observations or clusters that in some cases required a departure from the analysis procedure described above.

A115 (3C28.0): This cluster is undergoing a major off-axis merger, with the two subclusters separated by $300''$ (1 Mpc) in projection. The fainter southern subcluster

was manually excluded from our analysis. The *Chandra* observation of this system is discussed in detail by Gutierrez & Krawczynski (2005).

CLJ0152.7-1357: This system is dominated by a north-south merger between equal mass clusters whose cores are separated by $95''$ (720 kpc) in projection. The cluster is also associated with a network of large scale structure (Kodama et al. 2005; Maughan et al. 2006). The northern and southern subclusters (hereafter CLJ0152.7-1357N and CLJ0152.7-1357S) were analysed separately with the emission from each excluded during the analysis of the other.

MACSJ0329.7-0212: ObsIDs 3257 and 6108 were rejected due to background flaring, leaving ObsID 3582.

MACSJ0404.6+1109: An extended source at $\alpha[2000.0] = 4^{\text{h}}4^{\text{m}}42.85^{\text{s}}$ $\delta[2000.0] = +11^{\circ}09'39.6''$, $170''$ (0.9 Mpc) from the the cluster core, was manually excluded.

RXJ0439.0+0715: ObsID 526 was rejected due to a very high background level, leaving ObsID 3583.

1E0657-56: This cluster, a spectacular merger known as the ‘‘bullet cluster’’ (Markevitch et al. 2004), has been observed 10 times with *Chandra* ACIS-I for a total of > 500 ks. For simplicity we use only two of the observations in our analysis which total ~ 100 ks, which is more than sufficient for our purposes.

MACSJ0717.5+3745: ObsID 1655 was rejected due to a very high background level, leaving ObsID 4200.

MS0906.5+1110: This cluster is part of a structure that includes A750 ($\alpha[2000.0] = 09^{\text{h}}08^{\text{m}}59.25^{\text{s}}$ $\delta[2000.0] = +11^{\circ}02'39.9''$) at the same redshift. The centre of A750 is $300''$ (0.9 Mpc) from the core of MS0906.5+1110. The emission from A750 falls partially within the *Chandra* field of view in this observation and also within the R_{500} of MS0906.5+1110 and was manually excluded.

RXJ1234.2+0947: This system (also referred to as Z5247 in Ebeling et al. 1998) apparently consists of a binary merger between two clusters of similar mass. However, only one redshift is available in Ebeling et al. (1998) for this system, and the position given is that of the southern subcluster. The northern subcluster was thus manually excluded from the current analysis.

A1682: This cluster is part of a large scale filament comprising at least two other extended X-ray sources at the cluster redshift. These sources are at $\alpha[2000.0] = 13^{\text{h}}06^{\text{m}}58.52^{\text{s}}$ $\delta[2000.0] = +46^{\circ}31'37.5''$, and $\alpha[2000.0] = 13^{\text{h}}07^{\text{m}}13.33^{\text{s}}$ $\delta[2000.0] = +46^{\circ}29'08.4''$, and are $145''$ (0.5 Mpc) and $227''$ (0.8 Mpc) south east of the cluster core, respectively. These sources were manually excluded for the current analysis. Furthermore, the only ACIS-I observation of this cluster was affected by long, low level flares causing the background spectrum to differ significantly from the blank-sky background. For this reason, a local background was used for the spectral analysis.

CLJ1334+5031: The only ACIS-I observation of this cluster was affected by long, low level flares causing the background spectrum to differ significantly from the blank-sky background. For this reason, a local background was used for the spectral analysis.

A1763: An extended source at $\alpha[2000.0] = 13^{\text{h}}34^{\text{m}}53.21^{\text{s}}$ $\delta[2000.0] = +40^{\circ}56'55.34''$, $326''$ (1.2 Mpc; $\sim R_{500}$) from the the cluster core, was manually ex-

cluded.

A2069: An extended source at $\alpha[2000.0] = 15^{\text{h}}24^{\text{m}}27.70^{\text{s}}$ $\delta[2000.0] = +30^{\circ}01'44.29''$, $530''$ (1.1 Mpc; $\sim R_{500}$) from the the cluster core, was manually excluded.

RXJ1524.6+0957: This cluster is in a region of high Galactic X-ray emission at the base of the north polar spur, and thus had an extremely strong background residual spectrum. A cool APEC model at 0.30 keV was required to fit this soft foreground component.

A2111: An extended source at $\alpha[2000.0] = 15^{\text{h}}39^{\text{m}}32.70^{\text{s}}$ $\delta[2000.0] = +34^{\circ}28'07.37''$, $210''$ (0.8 Mpc) from the the cluster core, was manually excluded.

A2163: The lightcurve of ObsID 1653 was cleaned by hand to remove a long, low-level background flare.

MACSJ1621.3+3810: The lightcurve of ObsID 3594 was cleaned by hand to remove several periods of very high background.

MS1621.5+2640: An extended source at $\alpha[2000.0] = 16^{\text{h}}23^{\text{m}}48.25^{\text{s}}$ $\delta[2000.0] = +26^{\circ}34'22.11''$, $189''$ (1.1 Mpc; $\sim R_{500}$) from the the cluster core, was manually excluded.

RXJ1701+6414: This cluster (at $z = 0.453$) is separated by $285''$ in projection from the foreground cluster A2246 at $z = 0.225$. A2246 was manually excluded for this analysis. The observation was also affected by long, low level flares causing the background spectrum to differ significantly from the blank-sky background. For this reason, a local background was used for the spectral analysis.

A2261: An extended source at $\alpha[2000.0] = 17^{\text{h}}22^{\text{m}}12.15^{\text{s}}$ $\delta[2000.0] = +32^{\circ}06'54.0''$, $200''$ (0.7 Mpc) from the the cluster core, was manually excluded.

7. RESULTS AND DISCUSSION

7.1. Cluster morphologies

We have used two simple quantities (ellipticity and centroid shift) to measure the morphology of the clusters in the sample. In Fig. 5 we plot the clusters on the plane of these two quantities. The dashed lines indicate the median values for the entire sample. For some nearby clusters, R_{500} was not completely contained within the field of view, so R_w (the maximum radius within which $\langle w \rangle$ could be measured) was less than R_{500} . The 10 clusters for which $R_w < 0.9R_{500}$ were rejected from this morphological study to ensure uniformity. Broadly speaking, clusters to the bottom left of Fig. 5 are the most relaxed, with undisturbed, circular morphologies (*e.g.* A383) while those to the top left are elliptical clusters without significant substructure (*e.g.* A1413). The top right quadrant is home to clusters that are both elliptical and disturbed (*e.g.* CLJ0956+4107) and finally the bottom right quadrant contains disturbed clusters with broadly circular geometries (*e.g.* A520). Adaptively smoothed images of these four example clusters are plotted in Fig. 6

The sample was split into low and high-redshift subsets using a redshift cutoff of $z = 0.5$ and the two subsets are marked separately on Fig. 5. There is a clear absence of very relaxed clusters at $z > 0.5$, although the distribution of ellipticities does not vary significantly with redshift. The distribution of $\langle w \rangle$ alone is plotted in Fig. 7 for the low and high-redshift subsets. Again the ab-

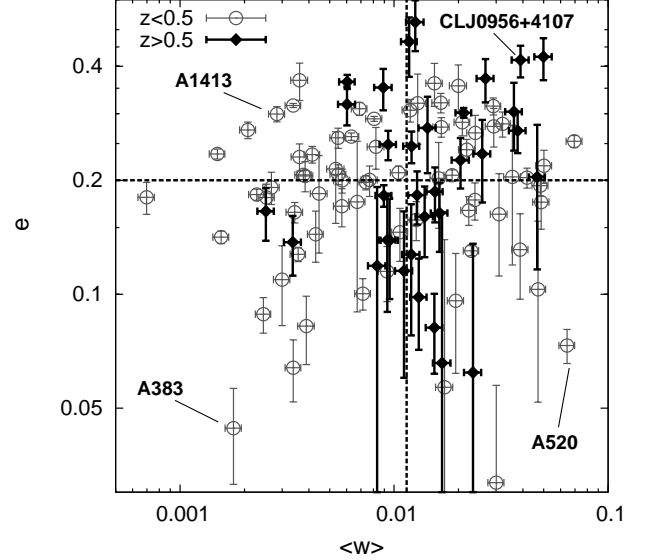


FIG. 5.— The clusters are plotted on the plane of centroid shift and ellipticity. The dashed lines show the median values of the full sample. Hollow and solid points show low and high-redshift clusters respectively.

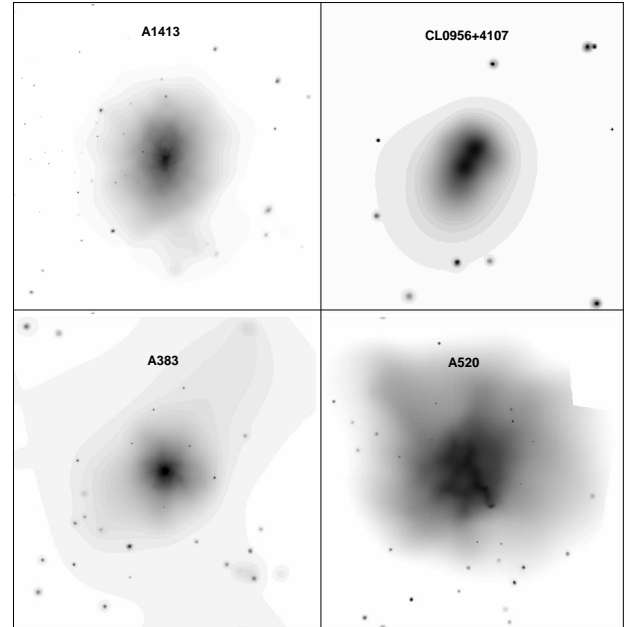


FIG. 6.— Adaptively smoothed images of clusters exemplifying the morphological characteristics potted in Fig 5. The clusters are plotted here in the same quadrants in which they reside in Fig 5.

sence of very relaxed clusters in the high-redshift subset is clear. A Kolmogorov-Smirnov test gave a probability that the two $\langle w \rangle$ subsets came from the same parent distribution of 4.5×10^{-4} ($> 3.5\sigma$). This reinforces, at greater significance, the results of Jeltema et al. (2005) who found more substructure in distant clusters than local clusters by using power ratios on *Chandra* images (see also Vikhlinin et al. 2006).

7.2. Evolution of metal abundance

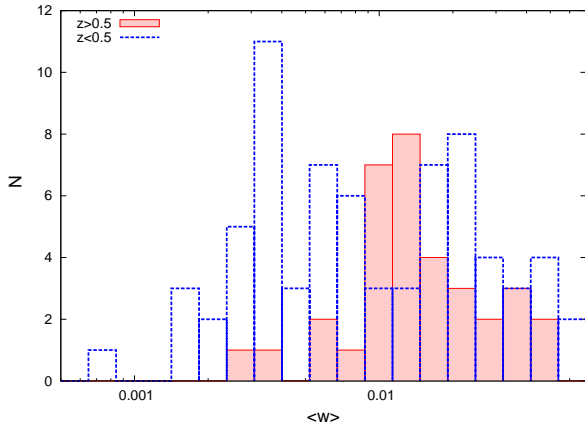


FIG. 7.— Histograms of the centroid shift parameter $\langle w \rangle$ for the low and high-redshift subsets of our sample.

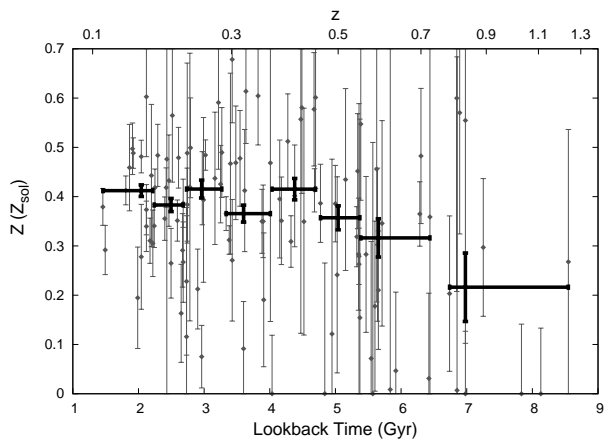


FIG. 8.— ICM metal abundances measured within R_{500} are plotted against lookback time and redshift for each cluster. All emission within R_{500} was used when measuring these abundances. The thick lines show the abundances measured from a joint fit to the clusters in different redshift bins. The bins contain ~ 15 clusters and the points are at the median redshift of each bin.

The abundance of metals in the ICM is the signature of star formation activity (and the ensuing supernovae) in the member galaxies, and the observed evolution of metal abundances can be used to trace the history of these processes (*e.g.* Ettori 2005; Balestra et al. 2006). Measuring metal abundances in distant clusters is challenging, and requires a higher quality of data than measuring temperature alone (see §7.5). In Fig. 8 we plot metal abundances measured within R_{500} as a function of redshift and lookback time. There are large uncertainties on the individual measurements, and for 9 clusters, the abundance measured was an upper limit. The abundance values are iron abundances relative to the solar values of Anders & Grevesse (1989). While these have been superseded by more recent measurements (*e.g.* Grevesse & Sauval 1998), they allow straightforward comparison with other works. A simple scaling of 0.676 converts from the Anders & Grevesse (1989) iron abundance to values relative to the Grevesse & Sauval (1998) abundances.

To improve the precision of the measurements, the clusters were grouped by redshift, and the spectra were fit simultaneously with the Galactic absorption, redshifts

and soft foreground component fixed at their measured values for each cluster. The model temperatures were free to fit independently for each cluster (but tied together for multiple observations of the same cluster) and the metal abundances were tied for all clusters in the group. The metal abundance measured for each group of clusters is then effectively a weighted mean, with the higher signal-to-noise (S/N) spectra naturally having a stronger weighting due to the χ^2 fitting method. The clusters were binned into groups of 15 clusters (with the highest redshift bin containing 11 clusters) and the abundances measured for each group are plotted with the unbinned data in Fig. 8. The locus of each bin is at the median redshift of the clusters in that bin.

The grouped abundances decrease with redshift from $\sim 0.4Z_{\odot}$ locally to $\sim 0.2Z_{\odot}$ at $z \approx 1$, with most of the decrease occurring at $z > 0.5$. The significance of the decrease was investigated by fitting a constant level to the grouped abundances. This model was rejected at the 99.9% level. Note that fitting a model to the unbinned data is problematic because of the upper limits at higher redshifts; a survival analysis that can include the upper limits correctly is not appropriate here, as it is not possible to include measurement errors in such analyses.

Clusters with cooling cores have been observed to have central peaks in their abundance profiles within $r \approx 150$ kpc, with abundances approaching solar values (De Grandi & Molendi 2001; Vikhlinin et al. 2005). Outside of the core the abundance profiles flatten significantly to values around $0.3Z_{\odot}$. De Grandi & Molendi (2001) also found significant (although much weaker) abundance gradients in non cool-core clusters. As the global abundances measured here are emission weighted, the sharp surface brightness peaks in cool-core clusters cause their central abundance peaks to be overrepresented in the global value, biasing it high. A similar, but much milder bias will also be present in the non cool-core clusters. It is therefore instructive to remove this effect by excising the core regions from the metal abundance measurements.

To this end, abundances were measured from spectra extracted in the annulus $(0.15 - 1)R_{500}$, although this leads to significantly lower signal to noise and hence larger uncertainties. The clusters were grouped as before and the spectra were fit simultaneously. The abundance evolution measured in this way is plotted in Fig. 9 along with the binned data from Fig. 8 (which show the abundances measured when the core region was not excluded). When the core regions are excluded, the data show the same trend of decreasing abundance with redshift, but at lower significance; the constant abundance model could only be rejected at the 87% level. The metal abundances are lower on average at all redshifts when the core was excluded, but the difference becomes less significant at $z > 0.5$. This can be partially explained by the decrease with redshift of the fraction of cool core clusters in the population (Vikhlinin et al. 2006). However, the data suggest that weak abundance gradients such as those found by De Grandi & Molendi (2001) in non cool-core clusters are still present at $z \sim 1$.

Our results are consistent with those of Balestra et al. (2006) based on a sample of 56 clusters observed in with *Chandra* (including many clusters in common with our

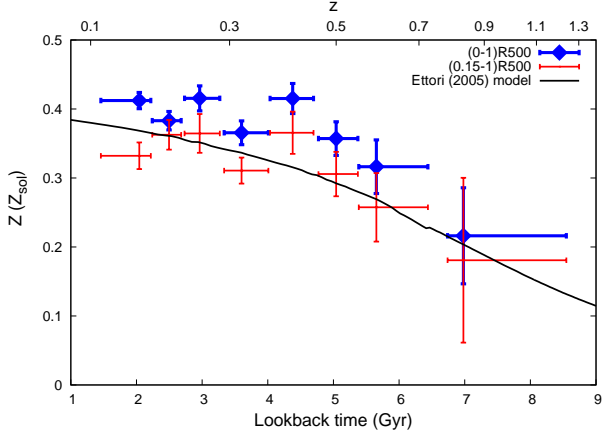


FIG. 9.— Mean ICM metal abundances measured from joint spectral fits to clusters grouped into redshift bins. Abundances measured in the $(0.15 - 1)R_{500}$ and $(0 - 1)R_{500}$ apertures are shown. The latter points are the same as those plotted in Fig. 8. The solid line shows the supernova enrichment model of Etti (2005).

sample). Key differences between these studies are the sizes of our samples, and the choice of spectral aperture. Balestra et al. (2006) used circular apertures in the approximate range $(0.3 - 0.6)R_{500}$ to maximise the S/N for each cluster, and included the core emission. We used the apertures $(0 - 1)R_{500}$ and $(0.15 - 1)R_{500}$ for all clusters. The Balestra et al. (2006) method has the advantage of yielding the most precise measurements for each cluster, while our method is consistent for all clusters, and allows us to address the effects of cool cores on the abundance measurements.

The overall decline in abundance with redshift that we observe is in qualitative agreement with the theoretical predictions of Etti (2005); the line in Fig. 9 is the solid line taken from their Fig. 5. The abundances measured with the cluster cores excluded agree well with the theoretical prediction, while those measured from the entire cluster are systematically higher than the model. This is likely to be due to the cool-core bias on our emission weighted global abundances. On the other hand, the abundances measured with the cores excluded will somewhat under-represent the true global value, because the higher metallicity gas in the cores is then ignored completely. It would be interesting to compare the evolution of mass-weighted abundances or total iron mass with theoretical predictions, but such measurements are not possible for the distant clusters with the current data.

7.3. Surface brightness profile slopes at large radii

The slope of the X-ray surface brightness profile is an important quantity because hydrostatic cluster masses derived within some radius depend on the slope of the gas density profile at that radius, which is measured from the surface brightness profile. The slope is often measured by fitting a simple β -model to the data, but this has been found to underestimate the slope of the data at large radii as the fit is driven by the higher S/N data in the inner parts of the profile (Vikhlinin et al. 1999). More recently, V06 demonstrated that much of the discrepancy between the normalisation of the mass-temperature relation from observational studies and simulations can be explained by underestimates of the gas density profile slope at large radii.

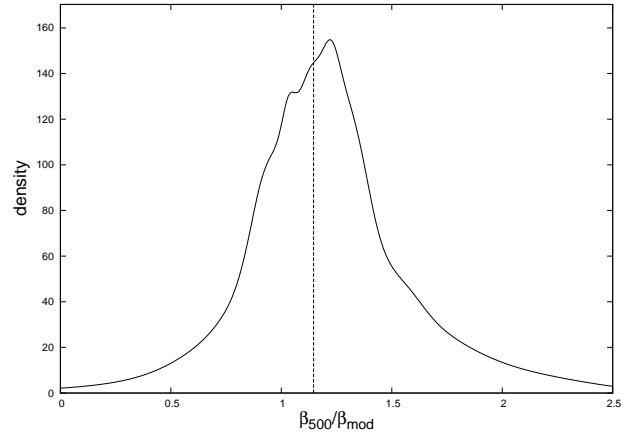


FIG. 10.— Kernel density plot of the ratio of the logarithmic slope of the observed surface brightness profiles at R_{500} to that of the best fitting β -model at the same radius. The dashed line shows the weighted mean.

The ratio β_{500}/β_{mod} was calculated for each cluster, and a kernel density plot of the population is shown in Fig. 10. To form this plot a Gaussian kernel was computed for each measurement with the central position and σ given by the measured β_{500}/β_{mod} and uncertainty. The kernels were normalised to have an area of unity and summed. The advantage of this plot over a histogram is that the uncertainties in the variable are included; well measured values contribute a high, narrow kernel while those with large uncertainties contribute a broad, low kernel. The resulting curve peaks at $\beta_{500}/\beta_{mod} = 1.2$ and the weighted mean of the values is 1.15. Thus, on average, the slope of the cluster surface brightness profiles at R_{500} is steeper by $\sim 15\%$ than the best-fitting β -model. This is consistent with the findings of Vikhlinin et al. (1999) and V06 and further reinforces the need for careful modelling of surface brightness profiles at large radii.

7.4. Similarity of surface brightness profiles

A simple and useful model of the structure of galaxy clusters is that they are self-similar. That is to say that clusters are identical when scaled appropriately by their mass. This would be the case if gravity were the only important factor in the formation, growth, and evolution of clusters. There are many examples of cluster properties deviating from self-similarity (e.g. Markevitch 1998; Ponman et al. 1999; Sanderson et al. 2003), but it remains a useful baseline model, and departures from self-similarity provide useful clues to non-gravitational processes that should be incorporated into cluster models. In the self-similar model, the surface brightness profiles of clusters should be identical, once scaled by mass. However, it has been established that there is a trend for cooler systems to exhibit shallower surface brightness profiles (e.g. Jones & Forman 1999; Vikhlinin et al. 1999; Sanderson et al. 2003). This demonstrates the increasing relative contribution of non-gravitational processes in clusters of lower masses.

The $\beta_{500} - kT$ relation was investigated for our sample and is plotted in Fig. 11. The best-fitting relations were measured with an orthogonal, weighted “BCES” regression (as described by Akritas & Bershady 1996), on the data in log space. The sample was divided at $z = 0.5$ into low and high-redshift subsets, and these were fit sep-

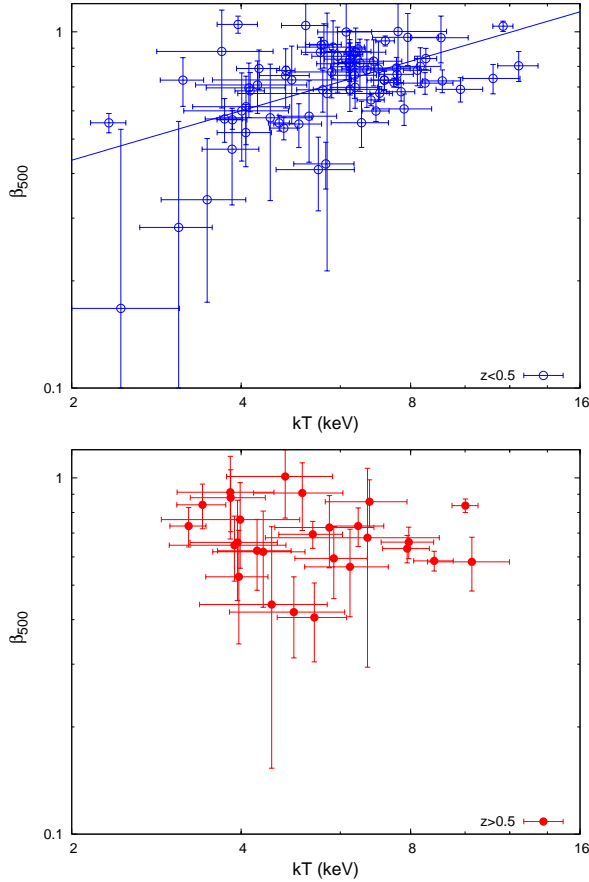


FIG. 11.— The $\beta_{500} - kT$ relations for the low-redshift (top) and high-redshift (bottom) subsets of the sample. The solid line in the top panel shows the best-fitting power law to that data.

arately and are plotted in Fig. 11. There was a significant trend for cooler clusters to have lower values of β_{500} in the low- z subset; the best fitting relation had a slope of 0.46 ± 0.09 . However, for the high-redshift subset, there was no significant correlation, the best-fitting slope was -0.1 ± 0.2 . The low-redshift slope is thus steeper than the high-redshift slope at the $\approx 2.5\sigma$ level. This is not simply due to the absence of cooler systems in the distant subset; the significance was unchanged when the systems cooler than 4 keV were excluded from the local subset. This result, while not strongly significant, could indicate that the self-similarity breaking is due to processes that become more important at lower redshifts. Alternatively, the possible flattening of the $\beta_{500} - kT$ relation with redshift could be related to the morphological evolution of the clusters. However, we find no correlation between β_{500} and $\langle w \rangle$ to support this hypothesis.

7.5. Dependence of spectral uncertainties on data quality

Finally, the large size of the sample enabled us to examine how the uncertainties on measured spectral properties depend on the signal to noise ratio of the spectra. Fig. 12 shows the fractional uncertainties on the temperature and metal abundance measured for the clusters plotted against the signal to noise (S/N) ratio in the spectral fitting band. There are certainly factors other than data quality that influence the measurement uncertainties, such as multiple temperature and abundance

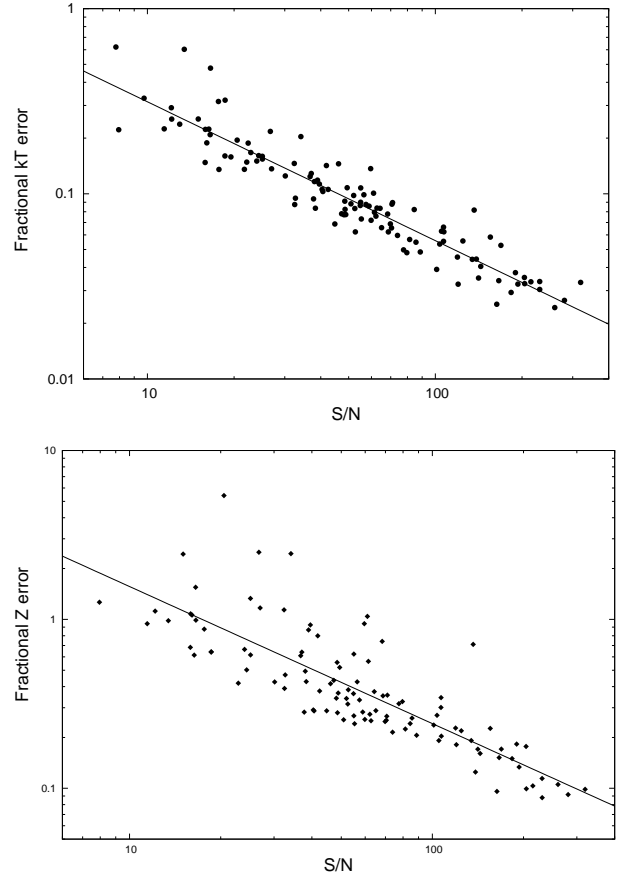


FIG. 12.— *Top*: Fractional kT errors versus spectrum signal to noise measured in the spectral fitting band. *Bottom*: Fractional Z errors versus spectrum signal to noise.

components and different levels of absorption. However, fairly tight power law correlations exist in both cases allowing us to define approximate relations that can be used for a “rule of thumb” assessment of data quality. We find $\sigma(kT)/kT = 1.77(S/N)^{-0.75}$ and $\sigma(Z)/Z = 10.0(S/N)^{-0.81}$.

8. SUMMARY AND CONCLUSIONS

We have performed a systematic analysis of the largest available sample of galaxy clusters at $z > 0.1$ observed with *Chandra* ACIS-I. Images and contour files are made available for each cluster. The structural properties and metal abundances of the clusters were investigated, and the main results can be summarised as follows:

- There is a significant absence of relaxed clusters at high redshift as measured by the centroid shifts of the cluster emission.
- The metal abundance of the ICM decreases with redshift, in line with theoretical predictions based on supernova rates.
- The abundance evolution is still present (although less significant) if the core regions of the clusters are excluded. This indicates that the observed evolution is not a result of the disappearance of cool-core clusters from the population at high redshifts.
- Metal abundances are lower at all redshifts when the cluster cores were excluded. This suggests that

weak abundance gradients are present in the ICM even at high redshifts where the influence of cool-cores is absent.

- The surface brightness slope at R_{500} (β_{500}) is steeper on average by $\sim 15\%$ than a simple β -model fit to the entire profile.
- There is a significant correlation between β_{500} and cluster temperature for local clusters, and an indication that the slope of this relation is shallower at high redshifts.

An important factor in these results is likely to be the higher cluster merger rate at high redshifts. This is predicted by cosmological simulations (*e.g.* Cohn & White 2005) and explains the absence of relaxed, cool-core clusters at $z \gtrsim 0.5$ (Jeltema et al. 2005; Vikhlinin et al. 2006). The changing cool-core population in turn has an effect on the metal abundance evolution, both because the metal abundances in the cool cores is higher and because the high emissivity of those regions then biases the the global emission-weighted abundances towards higher values. The fact that the evolution is also present when the cores are excluded suggests that the influence of cool cores is not the only effect. Indeed, the observed evolution agrees with that predicted by Ettori (2005) based on models of the rates star formation and subsequent supernova feedback with redshift. Furthermore, enhanced star formation has been found in the central galaxies of some cool core clusters (*e.g.* Hicks & Mushotzky 2005). This suggests that cool cores could be directly influencing the rate of enrichment of the ICM, although the amount of cool-core induced star formation is not well constrained. Finally, if the slope of the $\beta_{500} - kT$ relation were confirmed to be shallower at $z \gtrsim 0.5$, then this would suggest that the breaking of self-similarity in the

surface-brightness profiles was due to processes that become important at lower redshifts. This could be related to the onset at lower redshifts of cooling cores and their regulation by AGN outbursts (*e.g.* Nulsen et al. 2005).

As a final point, we remind the reader that the sample is not statistically complete, and is subject to the different selection processes by which the target clusters were originally chosen to be observed. As such, unquantifiable biases could be present, and so some caution is required in the interpretation of the results based on this sample. However, the agreement between the results presented here and other studies suggest that the impact of the heterogenous selection on our results is small. In subsequent papers we will use this large sample to study the cluster scaling relations, their evolution, departures from self-similarity, and the sources of scatter in the relations (*e.g.* Maughan 2007).

This research has made use of the X-Rays Clusters Database (BAX) which is operated by the Laboratoire d'Astrophysique de Tarbes-Toulouse (LATT), under contract with the Centre National d'Etudes Spatiales (CNES). We also used the NASA/IPAC Extragalactic Database (NED) which is operated by the Jet Propulsion Laboratory, California Institute of Technology, under contract with the National Aeronautics and Space Administration. We thank Alexey Vikhlinin for providing some of the software used in this work and Diab Jerius for help assembling the list of clusters. BJM is supported by NASA through Chandra Postdoctoral Fellowship Award Number PF4-50034 issued by the Chandra X-ray Observatory Center, which is operated by the Smithsonian Astrophysical Observatory for and on behalf of NASA under contract NAS8-03060.

REFERENCES

- Akritas M. G., Bershadsky M. A., 1996, *ApJ*, 470, 706
 Anders E., Grevesse N., 1989, *Geochim. Cosmochim. Acta*, 53, 197
 Balestra I., Tozzi P., Ettori S., Rosati P., Borgani S., Mainieri V., Norman C., Viola M., 2006, *ArXiv Astrophysics e-prints*
 Birkinshaw M., 1999, *Phys. Rep.*, 310, 97
 Bonamente M., Joy M. K., LaRoque S. J., Carlstrom J. E., Reese E. D., Dawson K. S., 2006, *ApJ*, 647, 25
 Buote D. A., Tsai J. C., 1995, *ApJ*, 452, 522
 Cavaliere A., Fusco-Femiano R., 1976, *A&A*, 49, L137
 Cohn J. D., White M., 2005, *Astroparticle Physics*, 24, 316
 De Grandi S., Molendi S., 2001, *ApJ*, 551, 153
 Dickey J. M., Lockman F. J., 1990, *ARA&A*, 28, 215
 Ebeling H., Edge A. C., Bohringer H., Allen S. W., Crawford C. S., Fabian A. C., Voges W., Huchra J. P., 1998, *MNRAS*, 301, 881
 Ebeling H., White D. A., Rangarajan F. V. N., 2006, *MNRAS*, 368, 65
 Ettori S., 2005, *MNRAS*, 362, 110
 Fabian A. C., 1994, *ARA&A*, 32, 277
 Grevesse N., Sauval A. J., 1998, *Space Science Reviews*, 85, 161
 Gutierrez K., Krawczynski H., 2005, *ApJ*, 619, 161
 Hicks A. K., Mushotzky R., 2005, *ApJ*, 635, L9
 Jeltema T. E., Canizares C. R., Bautz M. W., Buote D. A., 2005, *ApJ*, 624, 606
 Jones C., Forman W., 1984, *ApJ*, 276, 38
 Jones C., Forman W., 1999, *ApJ*, 511, 65
 Kaastra J. S., Mewe R., 1993, *A&AS*, 97, 443
 Kodama T., Tanaka M., Tamura T., Yahagi H., Nagashima M., Tanaka I., Arimoto N., 2005, *PASJ*, 57, 309
 Kravtsov A. V., Vikhlinin A., Nagai D., 2006, *ApJ*, 650, 128
 Lynds R., Petrosian V., 1989, *ApJ*, 336, 1
 Markevitch M., 1998, *ApJ*, 504, 27
 Markevitch M., Gonzalez A. H., Clowe D., Vikhlinin A., Forman W., Jones C., Murray S., Tucker W., 2004, *ApJ*, 606, 819
 Markevitch M., Ponman T. J., Nulsen P. E. J., Bautz M. W., Burke D. J., David L. P., Davis D., Donnelly R. H., Forman W. R., Jones C., et. al. 2000, *ApJ*, 541, 542
 Maughan B. J., Ellis S. C., Jones L. R., Mason K. O., Córdova F. A., Priedhorsky W., 2006, *ApJ*, 640, 219
 Maughan B. J., Jones C., Jones L. R., Van Speybroeck L., 2007, *ApJ*, 659, 1125
 Maughan B. J., 2007, *ApJ*, in press
 McNamara B. R., Wise M., Nulsen P. E. J., David L. P., Sarazin C. L., Bautz M., Markevitch M., Vikhlinin A., Forman W. R., Jones C., Harris D. E., 2000, *ApJ*, 534, L135
 Mohr J. J., Fabricant D. G., Geller M. J., 1993, *ApJ*, 413, 492
 Nulsen P. E. J., McNamara B. R., Wise M. W., David L. P., 2005, *ApJ*, 628, 629
 O'Hara T. B., Mohr J. J., Bialek J. J., Evrard A. E., 2006, *ApJ*, 639, 64
 Peres C. B., Fabian A. C., Edge A. C., Allen S. W., Johnstone R. M., White D. A., 1998, *MNRAS*, 298, 416
 Peterson J. R., Paerels F. B. S., Kaastra J. S., Arnaud M., Reiprich T. H., Fabian A. C., Mushotzky R. F., Jernigan J. G., Sakellou I., 2001, *A&A*, 365, L104
 Ponman T. J., Cannon D. B., Navarro J. F., 1999, *Nature*, 397, 135
 Poole G. B., Fardal M. A., Babul A., McCarthy I. G., Quinn T., Wadsley J., 2006, *MNRAS*, pp 1285+

- Pratt G. W., Arnaud M., 2002, *A&A*, 394, 375
- Sanderson A. J. R., Ponman T. J., Finoguenov A., Lloyd-Davies E. J., Markevitch M., 2003, *MNRAS*, 340, 989
- Sanderson A. J. R., Ponman T. J., O'Sullivan E., 2006, *MNRAS*, 372, 1496
- Sarazin C. L., 1986, *Reviews of Modern Physics*, 58, 1
- Smith R. K., Brickhouse N. S., Liedahl D. A., Raymond J. C., 2001, *ApJ*, 556, L91
- Snowden S. L., Egger R., Freyberg M. J., McCammon D., Plucinsky P. P., Sanders W. T., Schmitt J. H. M. M., Truemper J., Voges W., 1997, *ApJ*, 485, 125
- Tyson J. A., Wenk R. A., Valdes F., 1990, *ApJ*, 349, L1
- Vikhlinin A., Burenin R., Forman W. R., Jones C., Hornstrup A., Murray S. S., Quintana H., 2006, *ArXiv Astrophysics e-prints*
- Vikhlinin A., Forman W., Jones C., 1999, *ApJ*, 525, 47
- Vikhlinin A., Kravtsov A., Forman W., Jones C., Markevitch M., Murray S. S., Van Speybroeck L., 2006, *ApJ*, 640, 691
- Vikhlinin A., Markevitch M., Murray S. S., Jones C., Forman W., Van Speybroeck L., 2005, *ApJ*, 628, 655
- Vikhlinin A., McNamara B. R., Forman W., Jones C., Quintana H., Hornstrup A., 1998, *ApJ*, 502, 558
- Zwicky F., 1937, *ApJ*, 86, 217

TABLE 1
SUMMARY OF THE OBSERVATIONS USED. COLUMN 2 GIVES THE *Chandra* OBSERVATION IDENTIFIER, AND COLUMNS 3 AND 4 ARE THE ICRS EQUATORIAL COORDINATES OF THE CLUSTER X-RAY CENTROID. COLUMN 5 GIVES THE REDSHIFT OF EACH CLUSTER, AND COLUMNS 6 AND 7 GIVE THE DATE OF EACH OBSERVATION AND CORRESPONDING “BLANK-SKY” BACKGROUND PERIOD. FINALLY, COLUMN 8 LISTS THE CLEANED EXPOSURE TIME OF EACH OBSERVATION.

| Cluster | ObsID | RA | DEC | z | Date | BG | Exposure (ks) |
|------------------|-------|-------------|-------------|-------|------------|----|---------------|
| MS0015.9+1609 | 520 | 00:18:33.63 | +16:26:14.6 | 0.541 | 2000-08-18 | C | 55.7 |
| RXJ0027.6+2616 | 3249 | 00:27:45.92 | +26:16:19.9 | 0.367 | 2002-06-26 | D | 9.1 |
| CLJ0030+2618 | 5762 | 00:30:33.77 | +26:18:09.7 | 0.500 | 2005-05-28 | D | 16.1 |
| A68 | 3250 | 00:37:06.11 | +09:09:33.6 | 0.255 | 2002-09-07 | D | 7.3 |
| A115 | 3233 | 00:55:50.69 | +26:24:37.4 | 0.197 | 2002-10-07 | D | 43.6 |
| A209 | 3579 | 01:31:53.47 | -13:36:46.1 | 0.206 | 2003-08-03 | D | 8.8 |
| A209 | 522 | 01:31:53.59 | -13:36:46.1 | 0.206 | 2000-09-09 | C | 7.5 |
| CLJ0152.7-1357 | 913 | 01:52:40.03 | -13:58:24.2 | 0.831 | 2000-09-08 | C | 30.6 |
| A267 | 1448 | 01:52:42.12 | +01:00:41.4 | 0.230 | 1999-10-16 | B | 6.5 |
| MACSJ0159.8-0849 | 6106 | 01:59:49.32 | -08:50:00.7 | 0.405 | 2004-12-04 | D | 30.3 |
| MACSJ0159.8-0849 | 3265 | 01:59:49.44 | -08:50:00.6 | 0.405 | 2002-10-02 | D | 15.0 |
| CLJ0216-1747 | 6393 | 02:16:32.93 | -17:47:30.5 | 0.578 | 2005-10-04 | D | 20.0 |
| RXJ0232.2-4420 | 4993 | 02:32:18.34 | -44:20:50.3 | 0.284 | 2004-06-08 | D | 15.0 |
| MACSJ0242.5-2132 | 3266 | 02:42:35.86 | -21:32:25.8 | 0.314 | 2002-02-07 | D | 8.8 |
| A383 | 2320 | 02:48:03.43 | -03:31:46.2 | 0.187 | 2000-11-16 | C | 15.8 |
| A383 | 524 | 02:48:03.65 | -03:31:44.9 | 0.187 | 2000-09-08 | C | 8.8 |
| MACSJ0257.6-2209 | 3267 | 02:57:41.33 | -22:09:14.4 | 0.322 | 2001-11-12 | D | 16.6 |
| MS0302.7+1658 | 525 | 03:05:31.63 | +17:10:10.6 | 0.424 | 2000-10-03 | C | 9.1 |
| CLJ0318-0302 | 5775 | 03:18:33.60 | -03:02:55.3 | 0.370 | 2005-03-15 | D | 12.7 |
| MACSJ0329.6-0211 | 3582 | 03:29:41.54 | -02:11:45.9 | 0.450 | 2002-12-24 | D | 14.5 |
| MACSJ0404.6+1109 | 3269 | 04:04:32.66 | +11:08:16.8 | 0.355 | 2002-02-20 | D | 18.7 |
| MACSJ0429.6-0253 | 3271 | 04:29:35.95 | -02:53:06.1 | 0.399 | 2002-02-07 | D | 20.0 |
| RXJ0439.0+0715 | 3583 | 04:39:00.67 | +07:16:03.8 | 0.230 | 2003-01-04 | D | 16.1 |
| RXJ0439+0520 | 527 | 04:39:02.35 | +05:20:43.7 | 0.208 | 2000-08-29 | C | 8.0 |
| MACSJ0451.9+0006 | 5815 | 04:51:54.41 | +00:06:19.2 | 0.430 | 2005-01-08 | D | 8.0 |
| A521 | 901 | 04:54:06.58 | -10:13:15.2 | 0.253 | 1999-12-23 | B | 35.8 |
| A520 | 528 | 04:54:09.60 | +02:55:20.8 | 0.199 | 2000-10-10 | C | 8.5 |
| A520 | 4215 | 04:54:09.72 | +02:55:17.8 | 0.199 | 2003-12-04 | D | 48.7 |
| MS0451.6-0305 | 529 | 04:54:11.26 | -03:00:52.6 | 0.550 | 2000-01-14 | B | 12.7 |
| CLJ0522-3625 | 4926 | 05:22:14.66 | -36:24:58.7 | 0.472 | 2004-06-17 | D | 15.8 |
| CLJ0542.8-4100 | 914 | 05:42:50.14 | -41:00:02.2 | 0.634 | 2000-07-26 | C | 44.0 |
| MACSJ0647.7+7015 | 3584 | 06:47:49.92 | +70:14:56.0 | 0.584 | 2003-10-07 | D | 17.9 |
| MACSJ0647.7+7015 | 3196 | 06:47:50.16 | +70:14:55.7 | 0.584 | 2002-10-31 | D | 15.3 |
| 1E0657-56 | 3184 | 06:58:29.52 | -55:56:39.1 | 0.296 | 2002-07-12 | D | 69.5 |
| 1E0657-56 | 554 | 06:58:30.00 | -55:56:39.5 | 0.296 | 2000-10-16 | C | 22.3 |
| MACSJ0717.5+3745 | 4200 | 07:17:31.68 | +37:45:32.0 | 0.546 | 2003-01-08 | D | 51.8 |
| A586 | 530 | 07:32:20.16 | +31:37:54.5 | 0.171 | 2000-09-05 | C | 8.6 |
| MACSJ0744.9+3927 | 3585 | 07:44:52.32 | +39:27:25.2 | 0.697 | 2003-01-04 | D | 14.8 |
| MACSJ0744.9+3927 | 6111 | 07:44:52.32 | +39:27:27.0 | 0.697 | 2004-12-03 | D | 39.9 |
| MACSJ0744.9+3927 | 3197 | 07:44:52.56 | +39:27:26.3 | 0.697 | 2001-11-12 | D | 16.6 |
| A665 | 531 | 08:30:53.04 | +65:49:55.2 | 0.182 | 1999-12-29 | B | 7.8 |
| A665 | 3586 | 08:30:59.04 | +65:50:44.2 | 0.182 | 2002-12-28 | D | 26.2 |
| A697 | 4217 | 08:42:57.84 | +36:21:57.2 | 0.282 | 2002-12-15 | D | 16.1 |
| CLJ0848.7+4456 | 1708 | 08:48:47.76 | +44:56:12.5 | 0.574 | 2000-05-03 | C | 44.3 |
| CLJ0848.7+4456 | 927 | 08:48:50.88 | +44:55:27.8 | 0.574 | 2000-05-04 | C | 95.1 |
| ZWCLJ1953 | 1659 | 08:50:06.96 | +36:04:18.1 | 0.320 | 2000-10-22 | C | 17.9 |
| CLJ0853+5759 | 5765 | 08:53:14.64 | +57:59:47.8 | 0.475 | 2005-02-19 | D | 22.0 |
| CLJ0853+5759 | 4925 | 08:53:14.88 | +58:00:02.9 | 0.475 | 2004-09-19 | D | 14.3 |
| MS0906.5+1110 | 924 | 09:09:12.72 | +10:58:33.6 | 0.180 | 2000-10-02 | C | 26.4 |
| RXJ0910+5422 | 2452 | 09:10:44.40 | +54:22:04.4 | 1.110 | 2001-04-24 | D | 54.4 |
| RXJ0910+5422 | 2227 | 09:10:45.36 | +54:22:07.3 | 1.110 | 2001-04-29 | D | 84.2 |
| A773 | 5006 | 09:17:52.80 | +51:43:40.4 | 0.217 | 2004-01-21 | D | 15.8 |
| A773 | 3588 | 09:17:53.04 | +51:43:37.9 | 0.217 | 2003-01-25 | D | 8.8 |
| A773 | 533 | 09:17:53.04 | +51:43:39.4 | 0.217 | 2000-09-05 | C | 9.8 |
| A781 | 534 | 09:20:26.16 | +30:30:04.7 | 0.298 | 2000-10-03 | C | 8.6 |
| CLJ0926+1242 | 4929 | 09:26:36.48 | +12:43:04.8 | 0.489 | 2004-02-06 | D | 16.3 |
| CLJ0926+1242 | 5838 | 09:26:36.48 | +12:43:02.3 | 0.489 | 2005-02-21 | D | 27.2 |
| RBS797 | 2202 | 09:47:13.20 | +76:23:13.6 | 0.354 | 2000-10-20 | C | 9.8 |
| MACSJ0949.8+1708 | 3274 | 09:49:51.84 | +17:07:08.0 | 0.384 | 2002-11-06 | D | 12.9 |
| CLJ0956+4107 | 5759 | 09:56:03.12 | +41:07:14.2 | 0.587 | 2005-01-28 | D | 34.7 |
| CLJ0956+4107 | 5294 | 09:56:03.36 | +41:07:13.1 | 0.587 | 2003-12-30 | D | 13.5 |
| A907 | 535 | 09:58:21.84 | -11:03:49.0 | 0.153 | 2000-06-29 | C | 9.1 |
| A907 | 3205 | 09:58:22.08 | -11:03:49.3 | 0.153 | 2002-10-30 | D | 37.1 |
| A907 | 3185 | 09:58:22.08 | -11:03:50.0 | 0.153 | 2002-06-14 | D | 38.4 |
| MS1006.0+1202 | 925 | 10:08:47.52 | +11:47:40.6 | 0.221 | 2000-06-22 | C | 23.3 |
| MS1008.1-1224 | 926 | 10:10:32.16 | -12:39:30.2 | 0.301 | 2000-06-11 | C | 14.5 |
| ZW3146 | 909 | 10:23:39.60 | +04:11:11.3 | 0.291 | 2000-05-10 | C | 40.4 |
| CLJ1113.1-2615 | 915 | 11:13:05.28 | -26:15:41.0 | 0.725 | 2000-08-13 | C | 44.6 |
| A1204 | 2205 | 11:13:20.40 | +17:35:39.1 | 0.171 | 2001-06-01 | D | 19.4 |
| CLJ1117+1745 | 4933 | 11:17:30.00 | +17:44:52.1 | 0.305 | 2004-06-18 | D | 16.6 |

TABLE 1 — *Continued*

| Cluster | ObsID | RA | DEC | z | Date | BG | Exposure (ks) |
|------------------|-------|-------------|-------------|-------|------------|----|---------------|
| CLJ1117+1745 | 5836 | 11:17:30.00 | +17:44:52.8 | 0.548 | 2005-02-15 | D | 39.9 |
| CLJ1120+4318 | 5771 | 11:20:07.20 | +43:18:06.1 | 0.600 | 2005-01-11 | D | 16.6 |
| RXJ1121+2327 | 1660 | 11:20:57.36 | +23:26:29.0 | 0.562 | 2001-04-23 | D | 62.7 |
| A1240 | 4961 | 11:23:37.68 | +43:05:44.5 | 0.159 | 2005-02-05 | D | 43.5 |
| MACSJ1131.8-1955 | 3276 | 11:31:55.20 | -19:55:52.7 | 0.307 | 2002-06-14 | D | 11.1 |
| MS1137.5+6625 | 536 | 11:40:22.32 | +66:08:16.1 | 0.782 | 1999-09-30 | B | 103.1 |
| MACSJ1149.5+2223 | 3589 | 11:49:35.28 | +22:24:09.0 | 0.545 | 2003-02-07 | D | 15.0 |
| A1413 | 5003 | 11:55:18.00 | +23:24:17.6 | 0.143 | 2004-03-06 | D | 60.9 |
| A1413 | 1661 | 11:55:18.00 | +23:24:14.4 | 0.143 | 2001-05-16 | D | 9.3 |
| CLJ1213+0253 | 4934 | 12:13:35.04 | +02:53:46.4 | 0.409 | 2004-07-17 | D | 16.1 |
| CLJ1216+2633 | 4931 | 12:16:19.68 | +26:33:13.7 | 0.428 | 2004-05-12 | D | 15.3 |
| RXJ1221+4918 | 1662 | 12:21:26.40 | +49:18:28.1 | 0.700 | 2001-08-05 | D | 66.4 |
| CLJ1226.9+3332 | 5014 | 12:26:57.84 | +33:32:47.8 | 0.890 | 2004-08-07 | D | 25.1 |
| CLJ1226.9+3332 | 3180 | 12:26:57.84 | +33:32:47.8 | 0.890 | 2003-01-27 | D | 25.4 |
| RXJ1234.2+0947 | 539 | 12:34:18.00 | +09:46:18.8 | 0.229 | 2000-03-23 | C | 8.6 |
| RDSCS1252-29 | 4198 | 12:52:54.96 | -29:27:20.5 | 1.237 | 2003-03-20 | D | 133.2 |
| A1682 | 3244 | 13:06:51.12 | +46:33:29.5 | 0.234 | 2002-10-19 | D | 7.3 |
| MACSJ1311.0-0310 | 6110 | 13:11:01.68 | -03:10:37.6 | 0.494 | 2005-04-20 | D | 52.6 |
| MACSJ1311.0-0310 | 3258 | 13:11:01.92 | -03:10:36.0 | 0.494 | 2002-12-15 | D | 13.0 |
| A1689 | 5004 | 13:11:29.52 | -01:20:29.8 | 0.183 | 2004-02-28 | D | 16.6 |
| A1689 | 1663 | 13:11:29.52 | -01:20:28.7 | 0.183 | 2001-01-07 | D | 8.8 |
| A1689 | 540 | 13:11:29.52 | -01:20:30.4 | 0.183 | 2000-04-15 | C | 8.8 |
| RXJ1317.4+2911 | 2228 | 13:17:20.88 | +29:11:15.0 | 0.805 | 2001-05-04 | D | 88.4 |
| CLJ1334+5031 | 5772 | 13:34:18.72 | +50:31:02.3 | 0.620 | 2005-08-05 | D | 15.3 |
| A1763 | 3591 | 13:35:18.24 | +40:59:59.3 | 0.223 | 2003-08-28 | D | 17.4 |
| RXJ1347.5-1145 | 3592 | 13:47:30.72 | -11:45:10.4 | 0.451 | 2003-09-03 | D | 45.9 |
| RXJ1350.0+6007 | 2229 | 13:50:48.72 | +60:07:02.6 | 0.804 | 2001-08-29 | D | 47.7 |
| CLJ1354-0221 | 5835 | 13:54:17.04 | -02:21:52.3 | 0.546 | 2005-05-17 | D | 29.8 |
| CLJ1354-0221 | 4932 | 13:54:17.28 | -02:21:44.8 | 0.546 | 2004-12-07 | D | 15.3 |
| CLJ1415.1+3612 | 4163 | 14:15:11.04 | +36:12:03.6 | 1.030 | 2003-09-16 | D | 72.9 |
| RXJ1416+4446 | 541 | 14:16:28.08 | +44:46:42.6 | 0.400 | 1999-12-02 | B | 27.7 |
| MACSJ1423.8+2404 | 1657 | 14:23:47.76 | +24:04:40.8 | 0.543 | 2001-06-01 | D | 16.9 |
| A1914 | 3593 | 14:26:01.20 | +37:49:34.0 | 0.171 | 2003-09-03 | D | 16.1 |
| A1914 | 542 | 14:26:01.20 | +37:49:35.4 | 0.171 | 1999-11-21 | B | 7.2 |
| A1942 | 3290 | 14:38:22.08 | +03:40:06.2 | 0.224 | 2002-03-13 | D | 52.6 |
| MS1455.0+2232 | 543 | 14:57:15.12 | +22:20:34.4 | 0.258 | 2000-05-19 | C | 9.6 |
| MS1455.0+2232 | 4192 | 14:57:15.12 | +22:20:34.8 | 0.258 | 2003-09-05 | D | 73.1 |
| RXJ1504-0248 | 4935 | 15:04:07.44 | -02:48:18.4 | 0.215 | 2004-01-07 | D | 12.2 |
| A2034 | 2204 | 15:10:12.48 | +33:30:28.4 | 0.113 | 2001-05-05 | D | 51.6 |
| A2069 | 4965 | 15:24:09.36 | +29:53:10.0 | 0.116 | 2004-05-31 | D | 53.4 |
| RXJ1525+0958 | 1664 | 15:24:39.84 | +09:57:42.6 | 0.516 | 2002-04-01 | D | 43.6 |
| RXJ1532.9+3021 | 1665 | 15:32:53.76 | +30:20:59.3 | 0.345 | 2001-09-06 | D | 8.8 |
| A2111 | 544 | 15:39:41.28 | +34:25:10.2 | 0.229 | 2000-03-22 | C | 9.1 |
| A2125 | 2207 | 15:41:08.64 | +66:15:51.8 | 0.246 | 2001-08-24 | D | 71.3 |
| A2163 | 545 | 16:15:45.60 | -06:08:56.5 | 0.203 | 2000-07-29 | C | 9.1 |
| MACSJ1621.3+3810 | 3254 | 16:21:24.72 | +38:10:07.3 | 0.463 | 2002-10-18 | D | 8.3 |
| MACSJ1621.3+3810 | 6109 | 16:21:24.72 | +38:10:10.2 | 0.463 | 2004-12-11 | D | 32.9 |
| MACSJ1621.3+3810 | 6172 | 16:21:24.72 | +38:10:09.5 | 0.463 | 2004-12-25 | D | 23.1 |
| MS1621.5+2640 | 546 | 16:23:35.28 | +26:34:19.9 | 0.426 | 2000-04-24 | C | 26.2 |
| A2204 | 6104 | 16:32:47.04 | +05:34:32.5 | 0.152 | 2004-09-20 | D | 9.1 |
| A2218 | 1666 | 16:35:52.08 | +66:12:34.6 | 0.176 | 2001-08-30 | D | 37.3 |
| A2218 | 1454 | 16:35:52.08 | +66:12:34.2 | 0.176 | 1999-10-19 | B | 10.1 |
| CLJ1641+4001 | 3575 | 16:41:52.80 | +40:01:40.4 | 0.464 | 2003-09-24 | D | 36.0 |
| RXJ1701+6414 | 547 | 17:01:23.04 | +64:14:11.4 | 0.453 | 2000-10-31 | C | 38.4 |
| RXJ1716.9+6708 | 548 | 17:16:49.44 | +67:08:26.9 | 0.813 | 2000-02-27 | C | 42.5 |
| A2259 | 3245 | 17:20:08.64 | +27:40:09.8 | 0.164 | 2002-09-16 | D | 7.8 |
| RXJ1720.1+2638 | 1453 | 17:20:10.08 | +26:37:30.0 | 0.164 | 1999-10-19 | B | 7.0 |
| RXJ1720.1+2638 | 3224 | 17:20:10.08 | +26:37:29.3 | 0.164 | 2002-10-03 | D | 18.4 |
| RXJ1720.1+2638 | 4361 | 17:20:10.08 | +26:37:29.3 | 0.164 | 2002-08-19 | D | 20.2 |
| MACSJ1720.2+3536 | 3280 | 17:20:16.56 | +35:36:21.6 | 0.387 | 2002-11-03 | D | 17.4 |
| A2261 | 5007 | 17:22:27.12 | +32:07:56.6 | 0.224 | 2004-01-14 | D | 19.7 |
| A2261 | 550 | 17:22:27.12 | +32:07:57.4 | 0.224 | 1999-12-11 | B | 8.3 |
| A2294 | 3246 | 17:24:09.60 | +85:53:11.0 | 0.178 | 2001-12-24 | D | 8.3 |
| MACSJ1824.3+4309 | 3255 | 18:24:18.96 | +43:09:49.0 | 0.487 | 2002-09-14 | D | 12.4 |
| MACSJ1931.8-2634 | 3282 | 19:31:49.68 | -26:34:32.9 | 0.352 | 2002-10-20 | D | 12.4 |
| RXJ2011.3-5725 | 4995 | 20:11:27.12 | -57:25:09.8 | 0.279 | 2004-06-08 | D | 21.8 |
| MS2053.7-0449 | 1667 | 20:56:21.12 | -04:37:47.2 | 0.583 | 2001-10-07 | D | 37.1 |
| MS2053.7-0449 | 551 | 20:56:21.12 | -04:37:46.6 | 0.583 | 2000-05-13 | C | 38.4 |
| MACSJ2129.4-0741 | 3595 | 21:29:25.92 | -07:41:30.0 | 0.594 | 2003-10-18 | D | 16.9 |
| RXJ2129.6+0005 | 552 | 21:29:40.08 | +00:05:19.6 | 0.235 | 2000-10-21 | C | 8.5 |
| A2409 | 3247 | 22:00:53.04 | +20:58:27.8 | 0.148 | 2002-10-08 | D | 9.1 |
| MACSJ2228.5+2036 | 3285 | 22:28:32.88 | +20:37:11.6 | 0.412 | 2003-01-22 | D | 16.1 |
| MACSJ2229.7-2755 | 3286 | 22:29:45.36 | -27:55:36.5 | 0.324 | 2002-11-13 | D | 12.7 |
| MACSJ2245.0+2637 | 3287 | 22:45:04.80 | +26:38:03.1 | 0.301 | 2002-11-24 | D | 12.7 |
| RXJ2247+0337 | 911 | 22:47:28.08 | +03:36:59.5 | 0.200 | 2000-05-11 | C | 41.5 |
| AS1063 | 4966 | 22:48:44.88 | -44:31:44.4 | 0.252 | 2004-05-17 | D | 22.3 |
| CLJ2302.8+0844 | 918 | 23:02:48.00 | +08:43:53.0 | 0.722 | 2000-08-05 | C | 87.9 |

TABLE 1 — *Continued*

| Cluster | ObsID | RA | DEC | z | Date | BG | Exposure (ks) |
|---------|-------|-------------|-------------|-------|------------|----|---------------|
| A2631 | 3248 | 23:37:37.92 | +00:16:07.5 | 0.273 | 2002-07-08 | D | 8.0 |

TABLE 2

STRUCTURAL PROPERTIES OF THE CLUSTERS. R_w IS THE MAXIMUM RADIUS WITHIN WHICH THE CENTROID SHIFT ($\langle w \rangle$) COULD BE MEASURED. β_{500} IS THE LOGARITHMIC SLOPE OF THE SURFACE BRIGHTNESS PROFILE AT R_{500} . FOR CLUSTERS MARKED WITH A \dagger , THE EMISSION WAS NOT DETECTED TO A LARGE ENOUGH RADIUS TO MEASURE β_{500} .

| Cluster | e | $\langle w \rangle$ ($10^{-2} R_{500}$) | R_w (R_{500}) | β_{500} |
|--------------------------|------------------------|---|---------------------|------------------------|
| MS0015.9+1609 | $0.18^{+0.01}_{-0.01}$ | 0.90 ± 0.08 | 1.00 | $0.58^{+0.04}_{-0.04}$ |
| RXJ0027.6+2616 | $0.20^{+0.05}_{-0.05}$ | 1.62 ± 0.14 | 1.00 | $0.62^{+0.14}_{-0.13}$ |
| CLJ0030+2618 | $0.30^{+0.06}_{-0.06}$ | 3.63 ± 0.33 | 1.00 | $0.68^{+0.47}_{-0.30}$ |
| A68 | $0.31^{+0.02}_{-0.02}$ | 1.19 ± 0.10 | 1.00 | $0.78^{+0.18}_{-0.16}$ |
| A115 | $0.25^{+0.01}_{-0.01}$ | 6.95 ± 0.59 | 1.00 | $0.64^{+0.02}_{-0.02}$ |
| A209 | $0.21^{+0.01}_{-0.01}$ | 0.55 ± 0.05 | 1.00 | $0.73^{+0.04}_{-0.04}$ |
| CLJ0152.7-1357S | $0.42^{+0.05}_{-0.06}$ | 4.99 ± 0.47 | 1.00 | $0.44^{+0.29}_{-0.28}$ |
| A267 | $0.28^{+0.02}_{-0.02}$ | 3.21 ± 0.28 | 1.00 | $0.79^{+0.10}_{-0.10}$ |
| CLJ0152.7-1357N | $0.06^{+0.07}_{-0.06}$ | 2.34 ± 0.22 | 1.00 | $0.91^{+0.21}_{-0.18}$ |
| MACSJ0159.8-0849 | $0.06^{+0.01}_{-0.01}$ | 0.34 ± 0.03 | 1.00 | $0.69^{+0.06}_{-0.05}$ |
| CLJ0216-1747 \dagger | $0.46^{+0.07}_{-0.09}$ | 1.18 ± 0.10 | 1.00 | ... |
| RXJ0232.2-4420 | $0.17^{+0.01}_{-0.01}$ | 2.24 ± 0.19 | 1.00 | $0.96^{+0.15}_{-0.14}$ |
| MACSJ0242.5-2132 | $0.00^{+0.18}_{-0.00}$ | 0.33 ± 0.03 | 1.00 | $0.91^{+0.18}_{-0.16}$ |
| A383 | $0.04^{+0.01}_{-0.01}$ | 0.18 ± 0.02 | 1.00 | $0.68^{+0.09}_{-0.08}$ |
| MACSJ0257.6-2209 | $0.14^{+0.02}_{-0.02}$ | 0.43 ± 0.04 | 1.00 | $0.83^{+0.13}_{-0.12}$ |
| MS0302.7+1658 | $0.36^{+0.05}_{-0.05}$ | 2.00 ± 0.18 | 1.00 | $0.28^{+0.27}_{-0.29}$ |
| CLJ0318-0302 | $0.16^{+0.05}_{-0.05}$ | 3.09 ± 0.28 | 1.00 | $0.57^{+0.26}_{-0.22}$ |
| MACSJ0329.6-0211 | $0.15^{+0.03}_{-0.03}$ | 1.38 ± 0.13 | 1.00 | $0.93^{+0.11}_{-0.10}$ |
| MACSJ0404.6+1109 | $0.28^{+0.03}_{-0.03}$ | 2.92 ± 0.25 | 1.00 | $0.43^{+0.06}_{-0.06}$ |
| MACSJ0429.6-0253 | $0.21^{+0.02}_{-0.02}$ | 0.38 ± 0.03 | 1.00 | $0.79^{+0.16}_{-0.14}$ |
| RXJ0439.0+0715 | $0.20^{+0.01}_{-0.01}$ | 0.57 ± 0.05 | 1.00 | $0.88^{+0.09}_{-0.09}$ |
| RXJ0439+0520 | $0.11^{+0.02}_{-0.03}$ | 0.30 ± 0.03 | 1.00 | $0.47^{+0.14}_{-0.14}$ |
| MACSJ0451.9+0006 | $0.00^{+0.61}_{-0.00}$ | 1.59 ± 0.14 | 1.00 | $0.70^{+0.13}_{-0.12}$ |
| A521 | $0.20^{+0.01}_{-0.01}$ | 4.18 ± 0.36 | 1.00 | $0.78^{+0.02}_{-0.02}$ |
| A520 | $0.07^{+0.01}_{-0.01}$ | 6.43 ± 0.54 | 1.00 | $0.94^{+0.03}_{-0.03}$ |
| MS0451.6-0305 | $0.25^{+0.02}_{-0.02}$ | 0.94 ± 0.08 | 1.00 | $0.73^{+0.09}_{-0.09}$ |
| CLJ0522-3625 | $0.32^{+0.06}_{-0.07}$ | 1.29 ± 0.12 | 1.00 | $0.88^{+0.31}_{-0.23}$ |
| CLJ0542.8-4100 | $0.27^{+0.03}_{-0.03}$ | 3.78 ± 0.34 | 1.00 | $0.56^{+0.16}_{-0.15}$ |
| MACSJ0647.7+7015 | $0.36^{+0.02}_{-0.02}$ | 0.62 ± 0.06 | 1.00 | $0.58^{+0.10}_{-0.10}$ |
| 1E0657-56 | $0.13^{+0.00}_{-0.00}$ | 2.29 ± 0.19 | 1.00 | $1.04^{+0.04}_{-0.03}$ |
| MACSJ0717.5+3745 | $0.30^{+0.01}_{-0.01}$ | 2.11 ± 0.18 | 1.00 | $0.84^{+0.04}_{-0.04}$ |
| A586 | $0.08^{+0.02}_{-0.02}$ | 0.26 ± 0.02 | 0.81 | $0.80^{+0.14}_{-0.12}$ |
| MACSJ0744.9+3927 | $0.11^{+0.02}_{-0.02}$ | 1.41 ± 0.13 | 1.00 | $0.65^{+0.04}_{-0.04}$ |
| A665 | $0.07^{+0.01}_{-0.01}$ | 3.40 ± 0.29 | 0.77 | $0.72^{+0.02}_{-0.02}$ |
| A697 | $0.23^{+0.01}_{-0.01}$ | 0.41 ± 0.03 | 1.00 | $0.73^{+0.05}_{-0.05}$ |
| CLJ0848.7+4456 | $0.34^{+0.05}_{-0.05}$ | 1.06 ± 0.10 | 1.00 | $0.28^{+0.17}_{-0.18}$ |
| ZWCLJ1953 | $0.18^{+0.02}_{-0.02}$ | 2.39 ± 0.20 | 1.00 | $0.84^{+0.12}_{-0.11}$ |
| CLJ0853+5759 | $0.36^{+0.05}_{-0.05}$ | 1.54 ± 0.14 | 1.00 | $0.67^{+0.54}_{-0.38}$ |
| MS0906.5+1110 | $0.19^{+0.01}_{-0.01}$ | 4.82 ± 0.42 | 0.95 | $0.54^{+0.04}_{-0.04}$ |
| RXJ0910+5422 \dagger | $0.07^{+0.10}_{-0.07}$ | 1.68 ± 0.16 | 1.00 | ... |
| A773 | $0.21^{+0.01}_{-0.01}$ | 1.05 ± 0.09 | 1.00 | $0.60^{+0.04}_{-0.04}$ |
| A781 | $0.13^{+0.03}_{-0.03}$ | 3.88 ± 0.34 | 1.00 | $0.55^{+0.08}_{-0.08}$ |
| CLJ0926+1242 | $0.37^{+0.04}_{-0.04}$ | 0.36 ± 0.03 | 1.00 | $0.60^{+0.17}_{-0.16}$ |
| RBS797 | $0.27^{+0.01}_{-0.01}$ | 0.21 ± 0.02 | 1.00 | $0.88^{+0.16}_{-0.14}$ |
| MACSJ0949.8+1708 | $0.15^{+0.02}_{-0.02}$ | 1.07 ± 0.09 | 1.00 | $0.61^{+0.06}_{-0.06}$ |
| CLJ0956+4107 | $0.42^{+0.04}_{-0.04}$ | 3.90 ± 0.36 | 1.00 | $0.66^{+0.22}_{-0.20}$ |
| A907 | $0.29^{+0.00}_{-0.00}$ | 0.81 ± 0.07 | 1.00 | $0.92^{+0.05}_{-0.04}$ |
| MS1006.0+1202 | $0.24^{+0.02}_{-0.02}$ | 2.19 ± 0.19 | 1.00 | $0.70^{+0.09}_{-0.09}$ |
| MS1008.1-1224 | $0.18^{+0.03}_{-0.03}$ | 4.87 ± 0.43 | 1.00 | $0.75^{+0.15}_{-0.13}$ |
| ZW3146 | $0.18^{+0.01}_{-0.01}$ | 0.23 ± 0.02 | 1.00 | $0.78^{+0.08}_{-0.07}$ |
| CLJ1113.1-2615 \dagger | $0.00^{+0.38}_{-0.00}$ | 0.88 ± 0.08 | 1.00 | ... |
| A1204 | $0.16^{+0.01}_{-0.01}$ | 0.34 ± 0.03 | 1.00 | $0.57^{+0.08}_{-0.08}$ |
| CLJ1117+1745 | $0.28^{+0.06}_{-0.07}$ | 1.43 ± 0.13 | 1.00 | $0.76^{+0.23}_{-0.19}$ |
| CLJ1120+4318 | $0.14^{+0.05}_{-0.05}$ | 0.93 ± 0.08 | 1.00 | $1.01^{+0.27}_{-0.21}$ |
| RXJ1121+2327 | $0.16^{+0.03}_{-0.03}$ | 1.39 ± 0.13 | 1.00 | $0.84^{+0.13}_{-0.12}$ |

TABLE 2 — *Continued*

| Cluster | e | $\langle w \rangle$ ($10^{-2} R_{500}$) | R_w (R_{500}) | β_{500} |
|-----------------------------|------------------------|---|---------------------|------------------------|
| A1240 | $0.28^{+0.02}_{-0.02}$ | 1.66 ± 0.15 | 1.00 | $1.05^{+0.06}_{-0.06}$ |
| MACSJ1131.8-1955 | $0.31^{+0.02}_{-0.02}$ | 2.91 ± 0.25 | 1.00 | $0.72^{+0.05}_{-0.05}$ |
| MS1137.5+6625 | $0.14^{+0.02}_{-0.03}$ | 0.34 ± 0.03 | 1.00 | $0.41^{+0.10}_{-0.10}$ |
| MACSJ1149.5+2223 | $0.25^{+0.02}_{-0.02}$ | 1.21 ± 0.10 | 1.00 | $0.66^{+0.07}_{-0.07}$ |
| A1413 | $0.32^{+0.00}_{-0.00}$ | 0.34 ± 0.03 | 0.90 | $0.67^{+0.03}_{-0.03}$ |
| CLJ1213+0253 [†] | $0.06^{+0.08}_{-0.06}$ | 1.72 ± 0.16 | 1.00 | ... |
| CLJ1216+2633 [†] | $0.18^{+0.08}_{-0.09}$ | 0.67 ± 0.06 | 1.00 | ... |
| RXJ1221+4918 | $0.18^{+0.03}_{-0.03}$ | 1.28 ± 0.12 | 1.00 | $0.69^{+0.06}_{-0.06}$ |
| CLJ1226.9+3332 [†] | $0.10^{+0.03}_{-0.03}$ | 1.30 ± 0.11 | 1.00 | ... |
| RXJ1234.2+0947 | $0.10^{+0.05}_{-0.05}$ | 4.71 ± 0.40 | 0.95 | $1.00^{+0.35}_{-0.25}$ |
| RDSCS1252-29 | $0.12^{+0.07}_{-0.12}$ | 0.83 ± 0.08 | 1.00 | $0.91^{+0.27}_{-0.21}$ |
| A1682 | $0.22^{+0.04}_{-0.04}$ | 3.92 ± 0.34 | 0.70 | $0.41^{+0.10}_{-0.09}$ |
| MACSJ1311.0-0310 | $0.08^{+0.02}_{-0.02}$ | 0.39 ± 0.03 | 1.00 | $1.00^{+0.30}_{-0.23}$ |
| A1689 | $0.13^{+0.01}_{-0.01}$ | 0.36 ± 0.03 | 1.00 | $0.84^{+0.06}_{-0.06}$ |
| RXJ1317.4+2911 | $0.52^{+0.07}_{-0.08}$ | 1.26 ± 0.12 | 1.00 | $1.22^{+0.70}_{-0.39}$ |
| CLJ1334+5031 | $0.22^{+0.08}_{-0.09}$ | 1.70 ± 0.16 | 1.00 | $0.53^{+0.46}_{-0.40}$ |
| A1763 | $0.31^{+0.01}_{-0.01}$ | 0.69 ± 0.06 | 0.95 | $0.76^{+0.05}_{-0.05}$ |
| RXJ1347.5-1145 | $0.26^{+0.01}_{-0.01}$ | 0.63 ± 0.05 | 1.00 | $0.80^{+0.07}_{-0.07}$ |
| RXJ1350.0+6007 | $0.37^{+0.05}_{-0.05}$ | 2.67 ± 0.24 | 1.00 | $0.62^{+0.20}_{-0.18}$ |
| CLJ1354-0221 | $0.23^{+0.05}_{-0.06}$ | 2.58 ± 0.24 | 1.00 | $0.65^{+0.14}_{-0.13}$ |
| CLJ1415.1+3612 | $0.13^{+0.05}_{-0.05}$ | 1.20 ± 0.11 | 1.00 | $0.62^{+0.15}_{-0.13}$ |
| RXJ1416+4446 | $0.25^{+0.03}_{-0.03}$ | 0.82 ± 0.07 | 1.00 | $0.52^{+0.10}_{-0.10}$ |
| MACSJ1423.8+2404 | $0.17^{+0.03}_{-0.03}$ | 0.25 ± 0.02 | 1.00 | $0.59^{+0.14}_{-0.13}$ |
| A1914 | $0.16^{+0.01}_{-0.01}$ | 1.94 ± 0.16 | 0.81 | $1.37^{+0.19}_{-0.16}$ |
| A1942 | $0.11^{+0.02}_{-0.02}$ | 0.93 ± 0.08 | 1.00 | $0.57^{+0.03}_{-0.03}$ |
| MS1455.0+2232 | $0.21^{+0.01}_{-0.01}$ | 0.38 ± 0.03 | 1.00 | $0.55^{+0.03}_{-0.03}$ |
| RXJ1504-0248 | $0.23^{+0.01}_{-0.01}$ | 0.15 ± 0.01 | 1.00 | $0.80^{+0.11}_{-0.10}$ |
| A2034 | $0.15^{+0.01}_{-0.01}$ | 0.86 ± 0.07 | 0.81 | $0.90^{+0.04}_{-0.04}$ |
| A2069 | $0.37^{+0.01}_{-0.01}$ | 0.85 ± 0.07 | 0.74 | $0.82^{+0.05}_{-0.05}$ |
| RXJ1525+0958 | $0.23^{+0.03}_{-0.04}$ | 2.04 ± 0.19 | 1.00 | $0.73^{+0.10}_{-0.09}$ |
| RXJ1532.9+3021 | $0.18^{+0.02}_{-0.02}$ | 0.07 ± 0.01 | 1.00 | $0.69^{+0.09}_{-0.09}$ |
| A2111 | $0.28^{+0.02}_{-0.02}$ | 2.08 ± 0.18 | 1.00 | $0.56^{+0.08}_{-0.08}$ |
| A2125 | $0.32^{+0.02}_{-0.02}$ | 1.65 ± 0.15 | 1.00 | $0.56^{+0.03}_{-0.03}$ |
| A2163 | $0.17^{+0.01}_{-0.01}$ | 2.51 ± 0.20 | 0.63 | $1.48^{+0.15}_{-0.13}$ |
| MACSJ1621.3+3810 | $0.18^{+0.02}_{-0.02}$ | 0.25 ± 0.02 | 1.00 | $0.88^{+0.14}_{-0.12}$ |
| MS1621.5+2640 | $0.10^{+0.03}_{-0.03}$ | 1.94 ± 0.17 | 1.00 | $0.81^{+0.12}_{-0.11}$ |
| A2204 | $0.09^{+0.01}_{-0.01}$ | 0.25 ± 0.02 | 0.86 | $0.89^{+0.11}_{-0.10}$ |
| A2218 | $0.21^{+0.01}_{-0.01}$ | 1.87 ± 0.16 | 1.00 | $0.87^{+0.04}_{-0.04}$ |
| CLJ1641+4001 | $0.18^{+0.05}_{-0.06}$ | 0.45 ± 0.04 | 1.00 | $0.34^{+0.17}_{-0.16}$ |
| RXJ1701+6414 | $0.27^{+0.03}_{-0.03}$ | 1.39 ± 0.13 | 1.00 | $0.60^{+0.10}_{-0.10}$ |
| RXJ1716.9+6708 | $0.32^{+0.04}_{-0.04}$ | 0.60 ± 0.05 | 1.00 | $0.73^{+0.18}_{-0.15}$ |
| A2259 | $0.20^{+0.02}_{-0.02}$ | 0.77 ± 0.07 | 0.95 | $1.04^{+0.20}_{-0.16}$ |
| RXJ1720.1+2638 | $0.14^{+0.01}_{-0.01}$ | 0.16 ± 0.01 | 1.00 | $0.73^{+0.05}_{-0.05}$ |
| MACSJ1720.2+3536 | $0.17^{+0.02}_{-0.02}$ | 0.57 ± 0.05 | 1.00 | $0.97^{+0.17}_{-0.15}$ |
| A2261 | $0.10^{+0.01}_{-0.01}$ | 0.71 ± 0.06 | 1.00 | $0.68^{+0.04}_{-0.04}$ |
| A2294 | $0.07^{+0.02}_{-0.02}$ | 1.23 ± 0.10 | 0.77 | $1.22^{+0.32}_{-0.25}$ |
| MACSJ1824.3+4309 | $0.20^{+0.08}_{-0.08}$ | 3.57 ± 0.32 | 1.00 | $0.71^{+0.12}_{-0.12}$ |
| MACSJ1931.8-2634 | $0.30^{+0.01}_{-0.01}$ | 0.28 ± 0.02 | 1.00 | $0.69^{+0.10}_{-0.09}$ |
| RXJ2011.3-5725 | $0.00^{+0.44}_{-0.00}$ | 0.37 ± 0.03 | 1.00 | $0.73^{+0.12}_{-0.11}$ |
| MS2053.7-0449 | $0.14^{+0.04}_{-0.04}$ | 0.95 ± 0.09 | 1.00 | $0.53^{+0.19}_{-0.18}$ |
| MACSJ2129.4-0741 | $0.19^{+0.03}_{-0.03}$ | 1.56 ± 0.14 | 1.00 | $1.22^{+0.20}_{-0.17}$ |
| RXJ2129.6+0005 | $0.26^{+0.02}_{-0.02}$ | 0.55 ± 0.05 | 1.00 | $0.82^{+0.15}_{-0.13}$ |
| A2409 | $0.13^{+0.02}_{-0.02}$ | 1.08 ± 0.09 | 0.70 | $0.92^{+0.14}_{-0.12}$ |
| MACSJ2228.5+2036 | $0.03^{+0.03}_{-0.01}$ | 3.00 ± 0.26 | 1.00 | $0.79^{+0.06}_{-0.05}$ |
| MACSJ2229.7-2755 | $0.19^{+0.02}_{-0.02}$ | 0.27 ± 0.02 | 1.00 | $0.77^{+0.12}_{-0.11}$ |
| MACSJ2245.0+2637 | $0.23^{+0.02}_{-0.02}$ | 0.36 ± 0.03 | 1.00 | $0.58^{+0.15}_{-0.14}$ |
| RXJ2247+0337 | $0.21^{+0.05}_{-0.06}$ | 0.53 ± 0.05 | 1.00 | $0.17^{+0.34}_{-0.39}$ |
| AS1063 | $0.20^{+0.01}_{-0.01}$ | 0.74 ± 0.06 | 1.00 | $0.74^{+0.07}_{-0.07}$ |
| CLJ2302.8+0844 | $0.12^{+0.05}_{-0.06}$ | 1.11 ± 0.10 | 1.00 | $0.42^{+0.11}_{-0.11}$ |

TABLE 2 — *Continued*

| Cluster | e | $\langle w \rangle$ ($10^{-2} R_{500}$) | R_w (R_{500}) | β_{500} |
|---------|------------------------|---|---------------------|------------------------|
| A2631 | $0.22^{+0.02}_{-0.02}$ | 5.01 ± 0.43 | 1.00 | $0.76^{+0.11}_{-0.10}$ |

TABLE 3
SUMMARY OF THE CLUSTER PROPERTIES. CLUSTERS MARKED WITH A † WERE TOO FAINT TO PERMIT A FULL SPECTRAL FIT IN THE $(0.15 < r < 1)R_{500}$ APERTURE. FOR THESE CLUSTERS Y_X WAS DERIVED USING THE TEMPERATURE MEASURED IN THE $r < R_{500}$ APERTURE, AND L_X WAS MEASURED BY A SPECTRAL FIT IN THE $(0.15 < r < 1)R_{500}$ APERTURE WITH kT FIXED AT THE GLOBAL TEMPERATURE.

| Cluster | R_{500} (Mpc) | $r < R_{500}$ | | | | $(0.15 < r < 1)R_{500}$ | | | |
|------------------|--------------------|----------------------|--------------------------------------|------------------------|--|-------------------------|--------------------------------------|------------------------|----------------------------------|
| | | kT (keV) | L_X (10^{44} erg s $^{-1}$) | Z (Z_\odot) | M_{gas} ($10^{13}M_\odot$) | kT (keV) | L_X (10^{44} erg s $^{-1}$) | Z (Z_\odot) | Y_X ($10^{13}M_\odot$ keV) |
| MS0015.9+1609 | 1.24 | $9.0^{+0.5}_{-0.5}$ | 47.5 ± 0.7 | $0.32^{+0.06}_{-0.06}$ | $15.17^{+0.08}_{-0.11}$ | $8.9^{+0.6}_{-0.7}$ | 34.5 ± 0.6 | $0.24^{+0.07}_{-0.07}$ | $135.6^{+9.8}_{-10.1}$ |
| RXJ0027.6+2616 | 0.93 | $4.7^{+0.7}_{-0.7}$ | 6.6 ± 0.6 | $0.47^{+0.32}_{-0.28}$ | $4.60^{+0.14}_{-0.14}$ | $4.2^{+0.9}_{-0.5}$ | 5.0 ± 0.6 | $0.65^{+0.40}_{-0.33}$ | $19.1^{+4.3}_{-2.5}$ |
| CLJ0030+2618 | 0.93 | $4.8^{+1.3}_{-0.8}$ | 5.2 ± 0.6 | $0.82^{+0.54}_{-0.43}$ | $3.80^{+0.17}_{-0.18}$ | $4.7^{+1.5}_{-0.9}$ | 3.9 ± 0.6 | $1.02^{+0.74}_{-0.56}$ | $18.0^{+5.9}_{-3.6}$ |
| A68 | 1.19 | $8.1^{+0.9}_{-0.8}$ | 16.7 ± 0.6 | $0.39^{+0.17}_{-0.16}$ | $7.83^{+0.15}_{-0.13}$ | $6.5^{+1.0}_{-0.7}$ | 9.3 ± 0.5 | $0.46^{+0.22}_{-0.21}$ | $51.0^{+7.8}_{-5.7}$ |
| A115 | 1.25 | $5.3^{+0.1}_{-0.1}$ | 12.6 ± 0.1 | $0.36^{+0.04}_{-0.04}$ | $8.79^{+0.08}_{-0.08}$ | $7.1^{+0.4}_{-0.4}$ | 9.3 ± 0.1 | $0.30^{+0.07}_{-0.07}$ | $62.4^{+3.5}_{-3.4}$ |
| A209 | 1.30 | $7.1^{+0.4}_{-0.4}$ | 17.6 ± 0.3 | $0.26^{+0.07}_{-0.07}$ | $10.83^{+0.08}_{-0.09}$ | $7.3^{+0.5}_{-0.5}$ | 12.2 ± 0.3 | $0.29^{+0.10}_{-0.09}$ | $78.7^{+5.4}_{-5.3}$ |
| CLJ0152.7-1357S | 0.72 | $4.8^{+1.3}_{-0.8}$ | 7.6 ± 0.8 | $0.55^{+0.45}_{-0.37}$ | $3.38^{+0.17}_{-0.15}$ | $6.0^{+2.4}_{-1.8}$ | 6.0 ± 0.7 | $0.10^{+0.42}_{-0.10}$ | $20.2^{+8.2}_{-6.0}$ |
| A267 | 1.04 | $4.9^{+0.3}_{-0.3}$ | 11.1 ± 0.5 | $0.49^{+0.18}_{-0.17}$ | $5.74^{+0.10}_{-0.07}$ | $4.6^{+0.5}_{-0.4}$ | 7.0 ± 0.5 | $0.64^{+0.27}_{-0.24}$ | $26.5^{+2.6}_{-2.4}$ |
| CLJ0152.7-1357N | 0.78 | $5.3^{+0.8}_{-0.8}$ | 10.3 ± 0.6 | $0.00^{+0.13}_{-0.00}$ | $4.63^{+0.15}_{-0.14}$ | $5.3^{+1.0}_{-1.0}$ | 8.7 ± 0.7 | $0.03^{+0.27}_{-0.03}$ | $24.6^{+4.7}_{-4.5}$ |
| MACSJ0159.8-0849 | 1.28 | $7.9^{+0.3}_{-0.3}$ | 39.3 ± 0.5 | $0.31^{+0.05}_{-0.05}$ | $11.41^{+0.11}_{-0.07}$ | $9.9^{+0.9}_{-0.9}$ | 18.0 ± 0.4 | $0.05^{+0.10}_{-0.05}$ | $113.4^{+10.7}_{-13.5}$ |
| CLJ0216-1747 | 0.71 | $8.2^{+5.1}_{-16.0}$ | 2.8 ± 0.5 | $0.00^{+0.00}_{-0.00}$ | $1.87^{+0.09}_{-0.12}$ | $3.0^{+0.2}_{-0.2}$ | 1.4 ± 0.5 | $0.00^{+0.74}_{-0.00}$ | $5.6^{+1.3}_{-2.5}$ |
| RXJ0232.2-4420 | 1.34 | $7.9^{+0.4}_{-0.4}$ | 31.7 ± 0.6 | $0.49^{+0.09}_{-0.09}$ | $11.96^{+0.11}_{-0.19}$ | $9.2^{+1.1}_{-1.0}$ | 17.6 ± 0.5 | $0.41^{+0.16}_{-0.16}$ | $110.3^{+13.2}_{-12.6}$ |
| MACSJ0242.5-2132 | 1.09 | $4.8^{+0.2}_{-0.2}$ | 27.3 ± 0.7 | $0.48^{+0.10}_{-0.09}$ | $6.74^{+0.07}_{-0.21}$ | $5.9^{+0.9}_{-0.7}$ | 7.9 ± 0.4 | $0.08^{+0.18}_{-0.08}$ | $39.9^{+6.0}_{-5.1}$ |
| A383 | 0.98 | $3.9^{+0.1}_{-0.1}$ | 9.1 ± 0.2 | $0.48^{+0.06}_{-0.06}$ | $4.07^{+0.04}_{-0.04}$ | $4.2^{+0.4}_{-0.2}$ | 3.6 ± 0.1 | $0.35^{+0.12}_{-0.11}$ | $17.1^{+1.7}_{-0.8}$ |
| MACSJ0257.6-2209 | 1.14 | $7.4^{+0.6}_{-0.6}$ | 16.3 ± 0.5 | $0.41^{+0.12}_{-0.13}$ | $7.04^{+0.16}_{-0.07}$ | $6.9^{+1.1}_{-0.7}$ | 8.1 ± 0.3 | $0.17^{+0.17}_{-0.17}$ | $48.6^{+7.6}_{-7.2}$ |
| MS0302.7+1658 | 0.79 | $3.5^{+0.5}_{-0.4}$ | 6.0 ± 0.8 | $0.56^{+0.13}_{-0.34}$ | $2.98^{+0.13}_{-0.13}$ | $3.3^{+0.7}_{-0.5}$ | 3.2 ± 0.7 | $0.70^{+0.82}_{-0.56}$ | $10.0^{+2.4}_{-1.7}$ |
| CLJ0318-0302 | 0.88 | $4.0^{+0.6}_{-0.5}$ | 5.1 ± 0.3 | $0.00^{+0.12}_{-0.00}$ | $3.19^{+0.19}_{-0.13}$ | $4.3^{+0.7}_{-0.8}$ | 3.4 ± 0.2 | $0.00^{+0.08}_{-0.00}$ | $13.7^{+2.4}_{-2.5}$ |
| MACSJ0329.6-0211 | 0.99 | $4.5^{+0.3}_{-0.3}$ | 27.1 ± 0.9 | $0.58^{+0.12}_{-0.11}$ | $7.43^{+0.16}_{-0.17}$ | $4.4^{+0.5}_{-0.4}$ | 12.1 ± 0.6 | $0.35^{+0.18}_{-0.15}$ | $32.5^{+3.5}_{-3.4}$ |
| MACSJ0404.6+1109 | 1.07 | $5.9^{+0.7}_{-0.6}$ | 9.7 ± 0.4 | $0.19^{+0.14}_{-0.13}$ | $6.90^{+0.10}_{-0.14}$ | $5.9^{+0.8}_{-0.7}$ | 8.1 ± 0.4 | $0.13^{+0.15}_{-0.13}$ | $40.5^{+5.5}_{-4.7}$ |
| MACSJ0429.6-0253 | 1.12 | $5.4^{+0.4}_{-0.2}$ | 23.1 ± 0.6 | $0.51^{+0.10}_{-0.09}$ | $7.02^{+0.10}_{-0.10}$ | $6.8^{+1.1}_{-0.4}$ | 9.2 ± 0.4 | $0.39^{+0.18}_{-0.18}$ | $47.6^{+7.5}_{-4.3}$ |
| RXJ0439.0+0715 | 1.14 | $5.6^{+0.3}_{-0.3}$ | 15.7 ± 0.3 | $0.38^{+0.09}_{-0.07}$ | $7.19^{+0.09}_{-0.10}$ | $5.6^{+0.4}_{-0.4}$ | 8.7 ± 0.2 | $0.28^{+0.11}_{-0.10}$ | $40.2^{+4.3}_{-2.8}$ |
| RXJ0439+0520 | 0.94 | $3.8^{+0.2}_{-0.2}$ | 8.4 ± 0.4 | $0.56^{+0.14}_{-0.12}$ | $3.43^{+0.08}_{-0.06}$ | $3.8^{+0.5}_{-0.4}$ | 3.0 ± 0.3 | $0.35^{+0.26}_{-0.22}$ | $13.2^{+1.6}_{-1.5}$ |
| MACSJ0451.9+0006 | 0.97 | $5.6^{+0.8}_{-0.8}$ | 15.1 ± 0.8 | $0.35^{+0.23}_{-0.18}$ | $6.87^{+0.23}_{-0.16}$ | $4.8^{+1.0}_{-0.7}$ | 10.9 ± 0.8 | $0.44^{+0.32}_{-0.28}$ | $32.9^{+6.8}_{-4.8}$ |
| A521 | 1.18 | $5.1^{+0.2}_{-0.2}$ | 13.9 ± 0.3 | $0.42^{+0.07}_{-0.07}$ | $10.56^{+0.05}_{-0.09}$ | $5.0^{+0.2}_{-0.2}$ | 12.2 ± 0.2 | $0.43^{+0.08}_{-0.08}$ | $53.1^{+1.9}_{-1.9}$ |
| A520 | 1.31 | $7.1^{+0.2}_{-0.2}$ | 17.6 ± 0.2 | $0.42^{+0.04}_{-0.04}$ | $11.11^{+0.05}_{-0.07}$ | $7.2^{+0.3}_{-0.3}$ | 14.2 ± 0.1 | $0.43^{+0.05}_{-0.05}$ | $80.0^{+2.9}_{-3.0}$ |
| MS0451.6-0305 | 1.11 | $6.7^{+0.6}_{-0.5}$ | 39.9 ± 1.4 | $0.55^{+0.15}_{-0.15}$ | $12.08^{+0.16}_{-0.23}$ | $6.6^{+0.7}_{-0.6}$ | 28.8 ± 1.2 | $0.33^{+0.16}_{-0.15}$ | $80.1^{+8.7}_{-7.5}$ |
| CLJ0522-3625 | 0.77 | $3.8^{+0.9}_{-0.8}$ | 3.1 ± 0.3 | $0.00^{+0.27}_{-0.00}$ | $2.43^{+0.11}_{-0.14}$ | $3.4^{+0.9}_{-0.8}$ | 2.3 ± 0.3 | $0.00^{+0.16}_{-0.00}$ | $8.2^{+2.3}_{-1.9}$ |
| CLJ0542.8-4100 | 0.90 | $6.7^{+1.2}_{-0.9}$ | 9.9 ± 0.4 | $0.05^{+0.16}_{-0.05}$ | $4.92^{+0.10}_{-0.08}$ | $6.2^{+1.2}_{-2.0}$ | 7.5 ± 0.4 | $0.13^{+0.19}_{-0.13}$ | $30.7^{+5.8}_{-4.7}$ |
| MACSJ0647.7+7015 | 1.18 | $10.5^{+1.4}_{-1.0}$ | 42.4 ± 1.0 | $0.21^{+0.12}_{-0.13}$ | $11.59^{+0.16}_{-0.12}$ | $10.6^{+2.0}_{-1.4}$ | 22.1 ± 0.6 | $0.00^{+0.16}_{-0.00}$ | $122.4^{+23.4}_{-16.4}$ |
| 1E0657-56 | 1.58 | $11.7^{+0.4}_{-0.4}$ | 75.8 ± 0.5 | $0.31^{+0.03}_{-0.03}$ | $23.06^{+0.09}_{-0.10}$ | $11.7^{+0.5}_{-0.5}$ | 54.0 ± 0.4 | $0.33^{+0.04}_{-0.04}$ | $270.5^{+10.6}_{-10.6}$ |
| MACSJ0717.5+3745 | 1.36 | $10.5^{+0.6}_{-0.4}$ | 73.3 ± 0.9 | $0.28^{+0.06}_{-0.06}$ | $22.35^{+0.12}_{-0.12}$ | $10.1^{+0.5}_{-0.5}$ | 57.1 ± 0.8 | $0.32^{+0.06}_{-0.06}$ | $225.5^{+11.7}_{-11.6}$ |
| A586 | 1.16 | $6.6^{+0.4}_{-0.3}$ | 13.3 ± 0.3 | $0.60^{+0.12}_{-0.12}$ | $6.24^{+0.07}_{-0.07}$ | $6.4^{+0.6}_{-0.5}$ | 6.5 ± 0.3 | $0.84^{+0.23}_{-0.21}$ | $40.1^{+3.6}_{-3.2}$ |
| MACSJ0744.9+3927 | 1.04 | $7.6^{+0.4}_{-0.4}$ | 46.2 ± 1.3 | $0.36^{+0.07}_{-0.06}$ | $10.75^{+0.12}_{-0.14}$ | $7.7^{+0.6}_{-0.6}$ | 26.3 ± 1.0 | $0.31^{+0.09}_{-0.09}$ | $83.1^{+6.6}_{-6.5}$ |
| A665 | 1.37 | $7.5^{+0.2}_{-0.2}$ | 21.0 ± 0.2 | $0.34^{+0.04}_{-0.04}$ | $12.77^{+0.05}_{-0.07}$ | $7.5^{+0.3}_{-0.3}$ | 15.2 ± 0.2 | $0.34^{+0.06}_{-0.05}$ | $96.0^{+3.7}_{-3.7}$ |
| A697 | 1.41 | $9.0^{+0.6}_{-0.5}$ | 36.5 ± 0.6 | $0.43^{+0.08}_{-0.08}$ | $15.57^{+0.17}_{-0.12}$ | $8.8^{+0.7}_{-0.6}$ | 24.4 ± 0.5 | $0.47^{+0.10}_{-0.10}$ | $137.1^{+11.2}_{-10.0}$ |
| CLJ0848.7+4456 | 0.58 | $2.5^{+0.5}_{-0.4}$ | 1.1 ± 0.1 | $0.07^{+0.24}_{-0.07}$ | $1.06^{+0.04}_{-0.03}$ | $2.5^{+0.5}_{-0.5}$ | 0.8 ± 0.2 | $0.13^{+0.15}_{-0.13}$ | $2.6^{+0.5}_{-0.5}$ |
| ZWCLJ1953 | 1.12 | $7.3^{+0.7}_{-0.7}$ | 15.6 ± 0.4 | $0.09^{+0.10}_{-0.09}$ | $7.31^{+0.10}_{-0.08}$ | $6.2^{+0.7}_{-0.6}$ | 8.7 ± 0.3 | $0.15^{+0.14}_{-0.13}$ | $45.3^{+4.9}_{-4.8}$ |
| CLJ0853+5759 | 0.85 | $6.1^{+2.2}_{-1.4}$ | 3.2 ± 0.3 | $0.71^{+0.46}_{-0.41}$ | $2.69^{+0.14}_{-0.06}$ | $7.7^{+3.7}_{-2.5}$ | 3.0 ± 0.3 | $0.84^{+0.62}_{-0.51}$ | $20.7^{+10.1}_{-6.7}$ |
| MS0906.5+1110 | 1.06 | $5.3^{+0.2}_{-0.2}$ | 8.4 ± 0.1 | $0.31^{+0.07}_{-0.07}$ | $5.27^{+0.05}_{-0.04}$ | $4.8^{+0.3}_{-0.3}$ | 4.7 ± 0.1 | $0.22^{+0.08}_{-0.09}$ | $25.2^{+1.5}_{-1.4}$ |
| RXJ0910+5422† | 0.53 | $3.9^{+1.2}_{-1.0}$ | 2.9 ± 0.4 | $0.00^{+0.13}_{-0.00}$ | $1.41^{+0.07}_{-0.07}$ | ... | 2.2 ± 0.6 | ... | $5.8^{+2.1}_{-1.2}$ |
| A773 | 1.25 | $7.4^{+0.3}_{-0.3}$ | 17.2 ± 0.3 | $0.48^{+0.06}_{-0.06}$ | $9.09^{+0.06}_{-0.06}$ | $7.0^{+0.4}_{-0.4}$ | 10.9 ± 0.3 | $0.57^{+0.09}_{-0.08}$ | $63.9^{+3.8}_{-3.5}$ |
| A781 | 1.10 | $5.6^{+0.6}_{-0.6}$ | 10.8 ± 0.5 | $0.47^{+0.18}_{-0.17}$ | $7.80^{+0.14}_{-0.10}$ | $5.3^{+0.7}_{-0.4}$ | 9.2 ± 0.5 | $0.53^{+0.21}_{-0.19}$ | $41.7^{+5.9}_{-3.5}$ |
| CLJ0926+1242 | 0.81 | $4.5^{+0.8}_{-0.7}$ | 4.6 ± 0.3 | $0.24^{+0.20}_{-0.21}$ | $3.10^{+0.07}_{-0.07}$ | $5.1^{+1.0}_{-1.0}$ | 3.2 ± 0.2 | $0.00^{+0.25}_{-0.00}$ | $15.7^{+3.1}_{-3.2}$ |
| RBS797 | 1.13 | $6.0^{+0.3}_{-0.3}$ | 45.9 ± 0.9 | $0.35^{+0.07}_{-0.07}$ | $7.89^{+0.31}_{-0.18}$ | $6.3^{+0.9}_{-0.7}$ | 11.7 ± 0.6 | $0.54^{+0.23}_{-0.21}$ | $50.0^{+7.2}_{-5.9}$ |
| MACSJ0949.8+1708 | 1.23 | $8.0^{+0.7}_{-0.6}$ | 27.7 ± 0.8 | $0.40^{+0.12}_{-0.12}$ | $11.00^{+0.15}_{-0.09}$ | $7.7^{+0.9}_{-0.9}$ | 17.2 ± 0.6 | $0.27^{+0.15}_{-0.15}$ | $84.3^{+9.4}_{-9.4}$ |
| CLJ0956+4107 | 0.78 | $4.0^{+0.7}_{-0.5}$ | 5.3 ± 0.4 | $0.46^{+0.27}_{-0.23}$ | $3.15^{+0.09}_{-0.09}$ | $3.9^{+0.8}_{-0.6}$ | 4.2 ± 0.4 | $0.20^{+0.29}_{-0.20}$ | $12.3^{+2.6}_{-1.9}$ |
| A907 | 1.12 | $5.3^{+0.1}_{-0.1}$ | 10.4 ± 0.1 | $0.49^{+0.03}_{-0.03}$ | $5.44^{+0.03}_{-0.03}$ | $5.6^{+0.3}_{-0.3}$ | 4.8 ± 0.1 | $0.36^{+0.05}_{-0.05}$ | $30.6^{+1.4}_{-1.5}$ |
| MS1006.0+1202 | 1.11 | $5.9^{+0.4}_{-0.4}$ | 7.3 ± 0.2 | $0.16^{+0.10}_{-0.10}$ | $5.29^{+0.06}_{-0.06}$ | $6.3^{+0.6}_{-0.6}$ | 4.9 ± 0.2 | $0.09^{+0.14}_{-0.09}$ | $33.4^{+3.3}_{-3.2}$ |
| MS1008.1-1224 | 1.02 | $5.0^{+0.4}_{-0.4}$ | 9.7 ± 0.4 | $0.27^{+0.12}_{-0.12}$ | $5.60^{+0.10}_{-0.11}$ | $4.6^{+0.5}_{-0.4}$ | 6.4 ± 0.3 | $0.34^{+0.18}_{-0.16}$ | $26.0^{+2.7}_{-2.6}$ |
| ZW3146 | 1.30 | $6.4^{+0.1}_{-0.1}$ | 44.4 ± 0.4 | $0.37^{+0.03}_{-0.03}$ | $10.26^{+0.08}_{-0.10}$ | $8.2^{+0.4}_{-0.4}$ | 15.6 ± 0.3 | $0.22^{+0.08}_{-0.08}$ | $84.1^{+4.6}_{-4.6}$ |
| CLJ1113.1-2615 | 0.66 | $3.8^{+0.9}_{-0.7}$ | 3.7 ± 0.6 | $0.36^{+0.51}_{-0.36}$ | $1.80^{+0.09}_{-0.11}$ | $4.5^{+1.0}_{-1.1}$ | 2.1 ± 0.5 | $0.16^{+0.64}_{-0.16}$ | $8.2^{+1.9}_{-2.1}$ |
| A1204 | 0.92 | $3.4^{+0.1}_{-0.1}$ | 9.2 ± 0.2 | $0.37^{+0.05}_{-0.05}$ | $3.10^{+0.21}_{-0.06}$ | $3.8^{+0.3}_{-0.3}$ | 2.7 ± 0.1 | $0.13^{+0.10}_{-0.10}$ | $11.8^{+1.1}_{-0.8}$ |

TABLE 3 — *Continued*

| Cluster | R_{500} (Mpc) | $r < R_{500}$ | | | | $(0.15 < r < 1)R_{500}$ | | | |
|-----------------------------|--------------------|----------------------|--------------------------------------|------------------------|---|-------------------------|--------------------------------------|------------------------|-----------------------------------|
| | | kT (keV) | L_X (10^{44} erg s $^{-1}$) | Z (Z_\odot) | M_{gas} ($10^{13} M_\odot$) | kT (keV) | L_X (10^{44} erg s $^{-1}$) | Z (Z_\odot) | Y_X ($10^{13} M_\odot$ keV) |
| CLJ1117+1745 | 0.73 | $3.4^{+1.2}_{-0.6}$ | 2.0 ± 0.3 | $0.15^{+0.40}_{-0.15}$ | $2.00^{+0.05}_{-0.07}$ | $3.6^{+1.1}_{-0.8}$ | 1.7 ± 0.2 | $0.00^{+0.34}_{-0.00}$ | $7.2^{+2.2}_{-1.6}$ |
| CLJ1120+4318 | 0.88 | $4.9^{+0.7}_{-0.6}$ | 12.1 ± 0.8 | $0.35^{+0.21}_{-0.19}$ | $5.20^{+0.15}_{-0.11}$ | $4.9^{+1.1}_{-0.7}$ | 8.6 ± 0.7 | $0.19^{+0.27}_{-0.19}$ | $25.4^{+5.6}_{-3.9}$ |
| RXJ1121+2327 | 0.77 | $3.8^{+0.4}_{-0.3}$ | 4.7 ± 0.3 | $0.28^{+0.16}_{-0.14}$ | $3.29^{+0.05}_{-0.07}$ | $3.5^{+0.4}_{-0.3}$ | 4.2 ± 0.3 | $0.28^{+0.17}_{-0.15}$ | $11.7^{+1.3}_{-1.1}$ |
| A1240 | 0.92 | $3.9^{+0.7}_{-0.3}$ | 1.7 ± 0.1 | $0.19^{+0.12}_{-0.09}$ | $2.75^{+0.17}_{-0.03}$ | $3.9^{+1.1}_{-0.3}$ | 1.6 ± 0.1 | $0.18^{+0.15}_{-0.10}$ | $10.8^{+15.2}_{-0.9}$ |
| MACSJ1131.8-1955 | 1.35 | $8.3^{+0.5}_{-0.5}$ | 29.5 ± 0.7 | $0.47^{+0.11}_{-0.11}$ | $14.20^{+0.16}_{-0.16}$ | $9.1^{+1.0}_{-1.0}$ | 20.9 ± 0.6 | $0.41^{+0.22}_{-0.15}$ | $129.2^{+14.0}_{-14.0}$ |
| MS1137.5+6625 | 0.79 | $5.8^{+0.7}_{-0.6}$ | 12.2 ± 0.5 | $0.20^{+0.16}_{-0.15}$ | $3.99^{+0.06}_{-0.06}$ | $5.5^{+1.0}_{-0.6}$ | 7.1 ± 0.4 | $0.20^{+0.22}_{-0.20}$ | $21.8^{+4.1}_{-2.3}$ |
| MACSJ1149.5+2223 | 1.22 | $8.4^{+0.9}_{-0.7}$ | 40.8 ± 1.3 | $0.28^{+0.11}_{-0.11}$ | $15.49^{+0.27}_{-0.15}$ | $8.2^{+1.0}_{-0.8}$ | 32.6 ± 1.1 | $0.27^{+0.13}_{-0.13}$ | $127.8^{+16.3}_{-12.4}$ |
| A1413 | 1.26 | $7.2^{+0.2}_{-0.2}$ | 15.9 ± 0.1 | $0.41^{+0.03}_{-0.03}$ | $7.95^{+0.04}_{-0.05}$ | $7.0^{+0.3}_{-0.3}$ | 7.4 ± 0.1 | $0.34^{+0.05}_{-0.05}$ | $55.8^{+2.3}_{-2.1}$ |
| CLJ1213+0253 | 0.76 | $3.4^{+0.6}_{-0.5}$ | 1.9 ± 0.6 | $0.19^{+0.11}_{-0.09}$ | $1.99^{+0.11}_{-0.09}$ | $4.1^{+0.9}_{-0.9}$ | 1.4 ± 0.6 | $2.03^{+2.97}_{-1.36}$ | $8.2^{+1.8}_{-1.9}$ |
| CLJ1216+2633 [†] | 0.87 | $6.8^{+6.6}_{-2.2}$ | 3.2 ± 0.5 | $0.76^{+0.82}_{-0.65}$ | $2.48^{+0.13}_{-0.13}$ | ... | 3.1 ± 0.9 | ... | $15.5^{+7.2}_{-3.9}$ |
| RXJ1221+4918 | 0.86 | $5.8^{+0.6}_{-0.6}$ | 11.8 ± 0.5 | $0.48^{+0.14}_{-0.13}$ | $5.44^{+0.08}_{-0.07}$ | $5.7^{+0.7}_{-0.6}$ | 9.8 ± 0.4 | $0.48^{+0.15}_{-0.14}$ | $31.1^{+3.7}_{-3.5}$ |
| CLJ1226.9+3332 | 0.94 | $10.4^{+1.4}_{-1.0}$ | 43.5 ± 1.3 | $0.30^{+0.14}_{-0.14}$ | $7.94^{+0.22}_{-0.11}$ | $9.0^{+1.6}_{-1.3}$ | 21.7 ± 1.1 | $0.52^{+0.22}_{-0.22}$ | $71.3^{+13.1}_{-10.5}$ |
| RXJ1234.2+0947 | 1.17 | $6.7^{+2.3}_{-1.0}$ | 6.7 ± 0.3 | $0.12^{+0.25}_{-0.12}$ | $6.21^{+0.11}_{-0.09}$ | $7.7^{+1.7}_{-0.8}$ | 6.1 ± 0.2 | $0.00^{+0.26}_{-0.00}$ | $47.8^{+10.9}_{-13.9}$ |
| RDCS1252-29 | 0.52 | $4.8^{+0.8}_{-0.8}$ | 5.9 ± 0.7 | $0.27^{+0.24}_{-0.24}$ | $1.93^{+0.07}_{-0.07}$ | $4.3^{+0.8}_{-0.8}$ | 5.1 ± 0.6 | $0.36^{+0.31}_{-0.31}$ | $8.3^{+1.5}_{-1.5}$ |
| A1682 | 1.13 | $6.2^{+0.8}_{-0.8}$ | 10.0 ± 0.6 | $0.42^{+0.27}_{-0.25}$ | $7.07^{+0.13}_{-0.12}$ | $6.1^{+1.1}_{-0.9}$ | 7.5 ± 0.5 | $0.33^{+0.34}_{-0.30}$ | $42.9^{+7.9}_{-6.5}$ |
| MACSJ1311.0-0310 | 0.95 | $5.6^{+0.3}_{-0.3}$ | 16.2 ± 0.3 | $0.39^{+0.08}_{-0.07}$ | $4.59^{+0.11}_{-0.08}$ | $6.2^{+0.7}_{-0.7}$ | 6.7 ± 0.2 | $0.27^{+0.14}_{-0.14}$ | $28.6^{+3.2}_{-3.1}$ |
| A1689 | 1.37 | $9.0^{+0.3}_{-0.3}$ | 36.7 ± 0.3 | $0.42^{+0.04}_{-0.04}$ | $11.26^{+0.11}_{-0.06}$ | $8.4^{+0.4}_{-0.3}$ | 14.3 ± 0.2 | $0.40^{+0.07}_{-0.07}$ | $95.1^{+4.7}_{-3.7}$ |
| RXJ1317.4+2911 | 0.50 | $2.0^{+0.7}_{-0.5}$ | 1.2 ± 0.3 | $0.01^{+0.68}_{-0.01}$ | $0.95^{+0.06}_{-0.07}$ | $2.1^{+0.6}_{-0.5}$ | 1.0 ± 1.2 | $0.28^{+2.70}_{-0.28}$ | $2.0^{+35.5}_{-0.5}$ |
| CLJ1334+5031 [†] | 1.00 | $16.9^{+7.0}_{-3.6}$ | 11.8 ± 1.4 | $0.01^{+1.02}_{-0.01}$ | $4.83^{+0.25}_{-0.19}$ | ... | 12.4 ± 5.3 | ... | $38.1^{+12.3}_{-12.3}$ |
| A1763 | 1.32 | $7.8^{+0.4}_{-0.4}$ | 19.6 ± 0.3 | $0.29^{+0.07}_{-0.07}$ | $11.47^{+0.10}_{-0.07}$ | $7.7^{+0.5}_{-0.5}$ | 13.7 ± 0.3 | $0.26^{+0.09}_{-0.09}$ | $87.8^{+6.0}_{-5.9}$ |
| RXJ1347.5-1145 | 1.45 | $12.2^{+0.5}_{-0.5}$ | 145.4 ± 1.3 | $0.41^{+0.04}_{-0.04}$ | $19.45^{+0.11}_{-0.37}$ | $11.7^{+1.1}_{-1.1}$ | 38.3 ± 0.8 | $0.48^{+0.10}_{-0.10}$ | $227.6^{+21.3}_{-21.4}$ |
| RXJ1350.0+6007 [†] | 0.70 | $4.8^{+1.3}_{-0.9}$ | 5.6 ± 0.6 | $0.60^{+0.39}_{-0.33}$ | $2.78^{+0.11}_{-0.10}$ | ... | 4.6 ± 0.7 | ... | $12.2^{+2.4}_{-2.2}$ |
| CLJ1354-0221 | 0.76 | $3.8^{+0.8}_{-0.6}$ | 3.5 ± 0.3 | $0.26^{+0.33}_{-0.26}$ | $2.66^{+0.08}_{-0.05}$ | $3.1^{+0.5}_{-0.4}$ | 2.9 ± 0.4 | $0.55^{+0.44}_{-0.34}$ | $8.2^{+1.4}_{-1.1}$ |
| CLJ1415.1+3612 | 0.64 | $5.7^{+0.8}_{-0.7}$ | 11.3 ± 0.6 | $0.00^{+0.14}_{-0.00}$ | $3.15^{+0.08}_{-0.07}$ | $4.4^{+0.6}_{-0.6}$ | 7.4 ± 0.4 | $0.00^{+0.04}_{-0.00}$ | $13.8^{+1.6}_{-1.8}$ |
| RXJ1416+4446 | 0.86 | $3.7^{+0.3}_{-0.3}$ | 5.2 ± 0.4 | $0.91^{+0.30}_{-0.26}$ | $3.23^{+0.08}_{-0.05}$ | $4.3^{+0.5}_{-0.4}$ | 3.3 ± 0.4 | $1.07^{+0.48}_{-0.41}$ | $13.8^{+1.8}_{-1.3}$ |
| MACSJ1423.8+2404 | 0.99 | $5.9^{+0.5}_{-0.4}$ | 30.1 ± 1.0 | $0.45^{+0.12}_{-0.11}$ | $6.96^{+0.11}_{-0.17}$ | $5.7^{+0.9}_{-0.7}$ | 11.3 ± 0.7 | $0.43^{+0.23}_{-0.21}$ | $39.5^{+6.3}_{-5.1}$ |
| A1914 | 1.37 | $9.8^{+0.3}_{-0.3}$ | 32.6 ± 0.3 | $0.34^{+0.05}_{-0.05}$ | $10.69^{+0.09}_{-0.07}$ | $8.9^{+0.6}_{-0.6}$ | 12.4 ± 0.2 | $0.28^{+0.09}_{-0.09}$ | $94.8^{+6.4}_{-5.9}$ |
| A1942 | 0.94 | $4.3^{+0.3}_{-0.2}$ | 3.9 ± 0.1 | $0.27^{+0.08}_{-0.08}$ | $3.59^{+0.03}_{-0.03}$ | $3.9^{+0.2}_{-0.2}$ | 2.9 ± 0.1 | $0.20^{+0.09}_{-0.08}$ | $13.8^{+0.9}_{-0.9}$ |
| MS1455.0+2232 | 1.04 | $4.5^{+0.1}_{-0.1}$ | 20.2 ± 0.2 | $0.48^{+0.03}_{-0.03}$ | $5.62^{+0.10}_{-0.09}$ | $4.7^{+0.2}_{-0.2}$ | 6.3 ± 0.1 | $0.40^{+0.06}_{-0.06}$ | $26.2^{+1.2}_{-1.1}$ |
| RXJ1504-0248 | 1.34 | $6.8^{+0.2}_{-0.2}$ | 61.1 ± 0.6 | $0.35^{+0.04}_{-0.04}$ | $10.90^{+0.04}_{-0.47}$ | $8.3^{+0.8}_{-0.7}$ | 14.3 ± 0.4 | $0.35^{+0.14}_{-0.13}$ | $90.2^{+8.5}_{-8.1}$ |
| A2034 | 1.22 | $6.7^{+0.2}_{-0.2}$ | 9.0 ± 0.1 | $0.38^{+0.04}_{-0.04}$ | $6.88^{+0.02}_{-0.03}$ | $6.4^{+0.2}_{-0.2}$ | 6.2 ± 0.1 | $0.36^{+0.05}_{-0.05}$ | $44.1^{+1.4}_{-1.4}$ |
| A2069 | 1.20 | $6.3^{+0.2}_{-0.2}$ | 6.1 ± 0.1 | $0.29^{+0.05}_{-0.05}$ | $6.56^{+0.03}_{-0.03}$ | $6.2^{+0.3}_{-0.3}$ | 5.1 ± 0.1 | $0.26^{+0.06}_{-0.05}$ | $40.8^{+1.7}_{-1.7}$ |
| RXJ1525+0958 | 0.80 | $5.2^{+0.5}_{-0.5}$ | 5.9 ± 0.3 | $0.43^{+0.18}_{-0.17}$ | $3.86^{+0.10}_{-0.06}$ | $5.4^{+1.1}_{-0.6}$ | 5.3 ± 0.3 | $0.39^{+0.20}_{-0.19}$ | $20.7^{+4.2}_{-2.4}$ |
| RXJ1532.9+3021 | 1.12 | $5.1^{+0.2}_{-0.2}$ | 35.9 ± 0.9 | $0.60^{+0.10}_{-0.10}$ | $7.56^{+0.15}_{-0.15}$ | $6.1^{+0.7}_{-0.7}$ | 12.3 ± 0.6 | $0.42^{+0.18}_{-0.18}$ | $46.3^{+5.4}_{-5.4}$ |
| A2111 | 1.18 | $6.8^{+0.9}_{-0.5}$ | 10.7 ± 0.4 | $0.23^{+0.15}_{-0.15}$ | $7.44^{+0.10}_{-0.05}$ | $6.6^{+0.9}_{-0.7}$ | 7.7 ± 0.3 | $0.20^{+0.19}_{-0.18}$ | $49.0^{+6.7}_{-5.1}$ |
| A2125 | 0.77 | $2.6^{+0.1}_{-0.1}$ | 1.7 ± 0.1 | $0.21^{+0.08}_{-0.07}$ | $2.19^{+0.03}_{-0.02}$ | $2.5^{+0.2}_{-0.2}$ | 1.5 ± 0.1 | $0.20^{+0.08}_{-0.07}$ | $5.4^{+0.4}_{-0.4}$ |
| A2163 | 1.86 | $15.5^{+0.9}_{-0.9}$ | 87.8 ± 1.3 | $0.43^{+0.09}_{-0.09}$ | $32.45^{+0.18}_{-0.24}$ | $15.5^{+1.2}_{-1.2}$ | 54.1 ± 1.2 | $0.48^{+0.13}_{-0.13}$ | $502.4^{+39.5}_{-39.1}$ |
| MACSJ1621.3+3810 | 1.01 | $6.3^{+0.3}_{-0.3}$ | 17.8 ± 0.6 | $0.39^{+0.08}_{-0.08}$ | $6.08^{+0.11}_{-0.10}$ | $6.1^{+0.6}_{-0.6}$ | 8.7 ± 0.5 | $0.26^{+0.12}_{-0.12}$ | $37.1^{+3.6}_{-3.5}$ |
| MS1621.5+2640 | 1.03 | $6.1^{+0.6}_{-0.6}$ | 10.0 ± 0.4 | $0.58^{+0.17}_{-0.16}$ | $6.10^{+0.11}_{-0.13}$ | $6.1^{+0.8}_{-0.7}$ | 7.8 ± 0.4 | $0.54^{+0.20}_{-0.19}$ | $37.1^{+4.7}_{-4.6}$ |
| A2204 | 1.37 | $6.8^{+0.3}_{-0.2}$ | 38.0 ± 0.4 | $0.50^{+0.05}_{-0.05}$ | $11.50^{+0.09}_{-0.20}$ | $7.4^{+0.6}_{-0.6}$ | 12.3 ± 0.3 | $0.32^{+0.12}_{-0.11}$ | $85.6^{+6.7}_{-6.8}$ |
| A2218 | 1.21 | $6.8^{+0.3}_{-0.2}$ | 13.1 ± 0.1 | $0.31^{+0.05}_{-0.04}$ | $7.78^{+0.02}_{-0.07}$ | $6.3^{+0.2}_{-0.2}$ | 8.3 ± 0.1 | $0.35^{+0.06}_{-0.06}$ | $49.3^{+1.9}_{-2.0}$ |
| CLJ1641+4001 | 0.74 | $3.0^{+0.4}_{-0.4}$ | 2.6 ± 0.4 | $0.89^{+0.49}_{-0.37}$ | $2.06^{+0.06}_{-0.06}$ | $2.9^{+0.3}_{-0.7}$ | 1.7 ± 0.4 | $0.41^{+0.48}_{-0.33}$ | $5.9^{+0.7}_{-1.4}$ |
| RXJ1701+6414 | 0.93 | $5.2^{+0.6}_{-0.4}$ | 7.5 ± 0.4 | $0.60^{+0.18}_{-0.17}$ | $4.21^{+0.08}_{-0.06}$ | $6.0^{+1.0}_{-0.9}$ | 5.3 ± 0.3 | $0.54^{+0.26}_{-0.23}$ | $25.4^{+4.1}_{-3.7}$ |
| RXJ1716.9+6708 | 0.78 | $6.5^{+1.1}_{-0.9}$ | 12.0 ± 0.8 | $0.57^{+0.25}_{-0.23}$ | $4.08^{+0.11}_{-0.13}$ | $5.4^{+1.1}_{-0.9}$ | 7.8 ± 0.7 | $0.74^{+0.38}_{-0.31}$ | $22.1^{+4.6}_{-3.6}$ |
| A2259 | 1.09 | $5.6^{+0.4}_{-0.4}$ | 8.5 ± 0.2 | $0.28^{+0.11}_{-0.10}$ | $5.29^{+0.08}_{-0.07}$ | $5.2^{+0.6}_{-0.4}$ | 5.2 ± 0.2 | $0.41^{+0.17}_{-0.16}$ | $27.7^{+3.3}_{-2.1}$ |
| RXJ1720.1+2638 | 1.24 | $6.1^{+0.1}_{-0.1}$ | 19.8 ± 0.2 | $0.48^{+0.03}_{-0.03}$ | $7.46^{+0.31}_{-0.01}$ | $7.2^{+0.4}_{-0.4}$ | 7.8 ± 0.2 | $0.45^{+0.07}_{-0.07}$ | $53.5^{+3.5}_{-2.8}$ |
| MACSJ1720.2+3536 | 1.16 | $6.1^{+0.4}_{-0.4}$ | 24.0 ± 0.6 | $0.35^{+0.09}_{-0.09}$ | $7.92^{+0.18}_{-0.13}$ | $7.8^{+1.0}_{-1.0}$ | 11.2 ± 0.5 | $0.44^{+0.20}_{-0.18}$ | $61.7^{+8.2}_{-7.8}$ |
| A2261 | 1.31 | $7.2^{+0.3}_{-0.3}$ | 26.6 ± 0.3 | $0.39^{+0.05}_{-0.05}$ | $11.15^{+0.06}_{-0.08}$ | $7.4^{+0.4}_{-0.4}$ | 13.5 ± 0.2 | $0.33^{+0.08}_{-0.08}$ | $82.2^{+4.6}_{-4.6}$ |
| A2294 | 1.30 | $9.0^{+0.8}_{-0.7}$ | 14.6 ± 0.4 | $0.44^{+0.14}_{-0.14}$ | $8.64^{+0.11}_{-0.09}$ | $8.6^{+1.2}_{-0.7}$ | 8.7 ± 0.3 | $0.23^{+0.18}_{-0.18}$ | $74.7^{+10.6}_{-6.1}$ |
| MACSJ1824.3+4309 | 0.84 | $3.7^{+0.8}_{-0.6}$ | 5.2 ± 0.6 | $0.12^{+0.35}_{-0.12}$ | $3.46^{+0.24}_{-0.11}$ | $3.9^{+1.0}_{-0.7}$ | 4.1 ± 0.6 | $0.40^{+0.53}_{-0.38}$ | $13.6^{+3.4}_{-2.4}$ |
| MACSJ1931.8-2634 | 1.13 | $5.4^{+0.3}_{-0.2}$ | 43.1 ± 0.8 | $0.35^{+0.06}_{-0.06}$ | $9.31^{+0.15}_{-0.13}$ | $5.8^{+0.6}_{-0.5}$ | 15.3 ± 0.5 | $0.11^{+0.10}_{-0.10}$ | $53.6^{+5.4}_{-5.0}$ |
| RXJ2011.3-5725 | 0.85 | $3.8^{+0.2}_{-0.2}$ | 6.4 ± 0.3 | $0.59^{+0.14}_{-0.12}$ | $2.98^{+0.05}_{-0.05}$ | $3.3^{+0.3}_{-0.3}$ | 3.0 ± 0.2 | $0.42^{+0.21}_{-0.18}$ | $9.9^{+0.9}_{-0.8}$ |
| MS2053.7-0449 | 0.75 | $4.1^{+0.4}_{-0.4}$ | 4.4 ± 0.3 | $0.18^{+0.17}_{-0.16}$ | $2.68^{+0.06}_{-0.06}$ | $4.2^{+0.9}_{-0.6}$ | 3.0 ± 0.3 | $0.10^{+0.21}_{-0.10}$ | $11.2^{+2.3}_{-1.6}$ |
| MACSJ2129.4-0741 | 1.12 | $9.4^{+1.3}_{-1.0}$ | 36.2 ± 1.3 | $0.30^{+0.23}_{-0.16}$ | $10.58^{+0.23}_{-0.21}$ | $8.4^{+1.3}_{-1.2}$ | 21.0 ± 1.0 | $0.40^{+0.13}_{-0.13}$ | $88.5^{+13.7}_{-13.1}$ |
| RXJ2129.6+0005 | 1.20 | $5.6^{+0.3}_{-0.3}$ | 20.2 ± 0.5 | $0.50^{+0.10}_{-0.10}$ | $8.02^{+0.14}_{-0.14}$ | $7.0^{+0.9}_{-0.7}$ | 9.7 ± 0.4 | $0.40^{+0.19}_{-0.18}$ | $56.3^{+7.2}_{-5.5}$ |
| A2409 | 1.16 | $5.5^{+0.3}_{-0.2}$ | 10.6 ± 0.2 | $0.46^{+0.09}_{-0.08}$ | $6.42^{+0.06}_{-0.07}$ | $5.7^{+0.4}_{-0.4}$ | 6.3 ± 0.2 | $0.32^{+0.12}_{-0.11}$ | $36.5^{+2.7}_{-2.5}$ |
| MACSJ2228.5+2036 | 1.23 | $7.7^{+0.6}_{-0.6}$ | 29.9 ± 0.7 | $0.40^{+0.10}_{-0.10}$ | $12.58^{+0.20}_{-0.18}$ | $7.5^{+0.8}_{-0.7}$ | 20.8 ± 0.6 | $0.41^{+0.13}_{-0.13}$ | $94.5^{+9.6}_{-9.4}$ |

TABLE 3 — *Continued*

| Cluster | R_{500} (Mpc) | $r < R_{500}$ | | | | $(0.15 < r < 1)R_{500}$ | | | |
|------------------|--------------------|----------------------|--------------------------------------|------------------------|---|-------------------------|--------------------------------------|------------------------|-----------------------------------|
| | | kT (keV) | L_X (10^{44} erg s $^{-1}$) | Z (Z_\odot) | M_{gas} ($10^{13} M_\odot$) | kT (keV) | L_X (10^{44} erg s $^{-1}$) | Z (Z_\odot) | Y_X ($10^{13} M_\odot$ keV) |
| MACSJ2229.7-2755 | 1.06 | $4.2^{+0.3}_{-0.2}$ | 19.5 ± 0.6 | $0.61^{+0.11}_{-0.10}$ | $5.86^{+0.11}_{-0.15}$ | $5.9^{+0.8}_{-0.8}$ | 6.9 ± 0.3 | $0.25^{+0.18}_{-0.17}$ | $34.6^{+4.8}_{-4.8}$ |
| MACSJ2245.0+2637 | 1.04 | $5.1^{+0.3}_{-0.3}$ | 16.5 ± 0.5 | $0.68^{+0.13}_{-0.12}$ | $5.62^{+0.12}_{-0.09}$ | $5.3^{+0.7}_{-0.5}$ | 6.9 ± 0.4 | $0.62^{+0.23}_{-0.21}$ | $29.6^{+3.9}_{-2.7}$ |
| RXJ2247+0337 | 0.62 | $2.2^{+0.5}_{-0.4}$ | 0.3 ± 0.1 | $0.48^{+0.49}_{-0.28}$ | $0.60^{+0.02}_{-0.03}$ | $2.2^{+0.9}_{-0.5}$ | 0.2 ± 0.1 | $0.35^{+0.81}_{-0.28}$ | $1.3^{+0.6}_{-0.3}$ |
| AS1063 | 1.42 | $11.1^{+0.8}_{-0.9}$ | 43.2 ± 0.6 | $0.08^{+0.06}_{-0.06}$ | $12.11^{+0.08}_{-0.09}$ | $10.4^{+1.4}_{-0.9}$ | 16.4 ± 0.4 | $0.13^{+0.13}_{-0.13}$ | $126.5^{+16.7}_{-10.9}$ |
| CLJ2302.8+0844 | 0.73 | $5.0^{+1.0}_{-0.7}$ | 4.7 ± 0.3 | $0.03^{+0.17}_{-0.03}$ | $2.61^{+0.06}_{-0.05}$ | $4.9^{+1.4}_{-1.0}$ | 3.3 ± 0.3 | $0.04^{+0.23}_{-0.04}$ | $12.7^{+3.6}_{-2.5}$ |
| A2631 | 1.22 | $6.5^{+0.5}_{-0.5}$ | 17.9 ± 0.6 | $0.44^{+0.13}_{-0.13}$ | $9.91^{+0.15}_{-0.21}$ | $6.5^{+0.6}_{-0.6}$ | 13.5 ± 0.5 | $0.43^{+0.16}_{-0.15}$ | $64.1^{+6.5}_{-5.7}$ |